DJO-2001

A High Performance Aircraft for the 2020 WPI UAV Competition

A Major Qualifying Project Report
Submitted to the Faculty of the
Worcester Polytechnic Institute
in Partial Fulfillment of the Requirements for the
Degree of Bachelor of Science in
Aerospace Engineering

by

Robert Bellitto

Keith Blackstock

Conor Blomquist

Marc Umbricht

May 11, 2020

Approved by:

David J. Olinger
Faculty Advisor, Associate Professor
Aerospace Engineering Program
WPI

Jagannath Jayachandran
Co-Faculty Advisor, Assistant Professor
Aerospace Engineering Program
WPI

Abstract

A fixed-wing drone for an internal Worcester Polytechnic Institute (WPI) sponsored flight competition was designed, constructed, and tested. The competition requirements reward maximizing flight range and payload fraction, autonomous operation, and require a payload release system to accurately hit a prescribed target. In this report we present our design process and discuss particular design innovations. The high lift-drag ratio aircraft uses a fiberglass sandwich composite wing combined with a foam-board panel fuselage to maximize weight savings and structural rigidity. The aircraft is catapult launched and uses landing gear that deploys automatically upon payload release. A waypoint navigation system with automatic payload release is also incorporated to improve the bombing accuracy.

Acknowledgments

We would like to thank the following individuals and groups for their help and support throughout this project:

- The WPI Aerospace Engineering Program
- Professor Olinger
- Professor Jayachandran
- Professor Cowlagi
- The Aerospace Engineering MQP Laboratory
- The WPI CollabLab
- Barbara Fuhrman, ME Department
- Millis Model RC Aircraft Club

Contents

Section	Author(s)
Introduction	Conor Blomquist, Marc Umbricht
1.1	March Umbricht
1.2	Conor Blomquist
1.3	Conor Blomquist
1.4	Conor Blomquist
1.5	Conor Blomquist
1.6	Conor Blomquist
Scoring Analysis	Marc Umbricht
2.1	Marc Umbricht
2.2	Marc Umbricht
2.3	Marc Umbricht
2.4	Marc Umbricht
Alternative Designs	Marc Umbricht, RJ Bellitto
3.1	Marc Umbricht
3.2	Marc Umbricht
3.3	RJ Bellitto
Analysis Methods	Marc Umbricht, Conor Blomquist, RJ Bellitto, Keith Blackstock
4.1	Marc Umbricht
4.2	Conor Blomquist, Marc Umbricht
4.3	Conor Blomquist, RJ Bellitto
4.4	Conor Blomquist
4.5	Marc Umbricht
4.6	Keith Blackstock, RJ Bellitto, Marc Umbricht, Conor Blomquist
4.7	RJ Bellitto
4.8	RJ Bellitto, Keith Blackstock, Conor Blomquist, Marc Umbricht
Summary, Conclusions, Reco's, Impacts	Conor Blomquist
5.1	Conor Blomquist
5.2	Conor Blomquist
5.3	Conor Blomquist
5.4	Conor Blomquist
Editing	Conor Blomquist, Marc Umbricht

Table 1: Table of Authorship

1 Introduction

A micro aerial vehicle (MAV) is a class of unmanned aerial vehicle (UAV) with a smaller size restriction. There are many purposes for these types of aircraft. For example, they can be used for aerial surveillance and reconnaissance of hazardous areas which would be dangerous for manned aircraft. Another popular use for MAV's is aerobatics. Smaller remote-controlled aircraft are much easier for use in aerobatic competitions compared to full size UAV's.

The primary goal of this project is to design and construct an MAV for use in the internal WPI competition. The aircraft must demonstrate that it is capable of flight through many tasks including takeoff, steady level flight, turns, a payload release, and landing. These goals will be achieved through flight testing once the final design is complete. The project as a whole consists of three separate MQP teams with two focusing on a fixed-wing aircraft and one focusing on a vertical takeoff and landing (VTOL) aircraft.

Figure 1 displays the main components of the final designed aircraft. Easily recognizable in the figure are the T-tail design, modular fuselage, payload bay doors, and an accurate model of the final wing. Figure 2 displays a top, side, and front view of the final aircraft design as well, highlighting the payload bay and t-tail design aspects. Finally, Figure 3 shows the finished aircraft on the day of the official flight test.

The objectives specific to this MQP are to perform structural, aerodynamic, stability, and propulsion analysis to develop a design for a fixed-wing MAV that complies with the competition rules set forth by the WPI faculty.

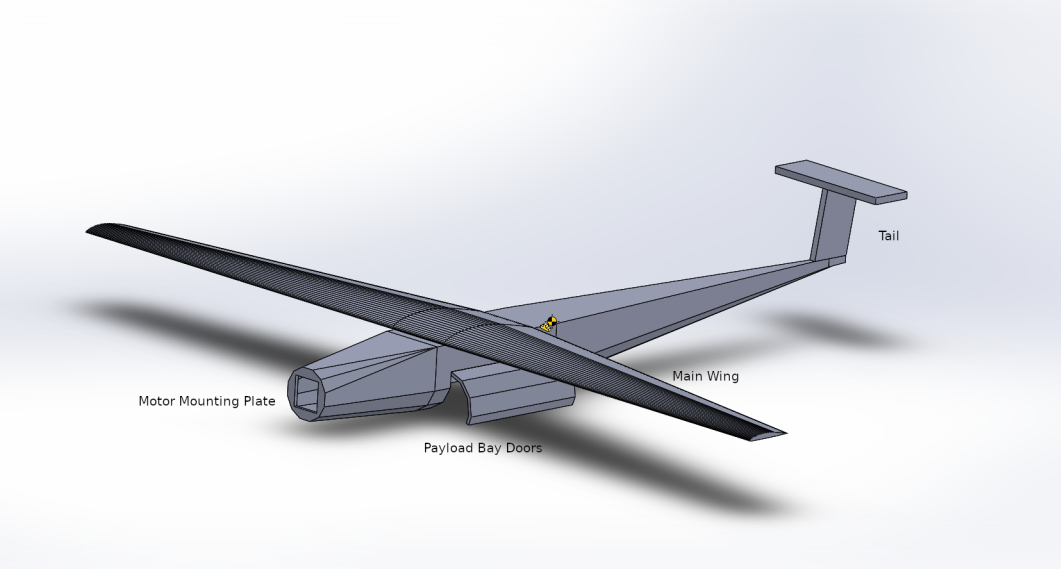

Figure 1: A SolidWorks rendering of the final aircraft design, shown here with payload doors open, but gear undeployed.

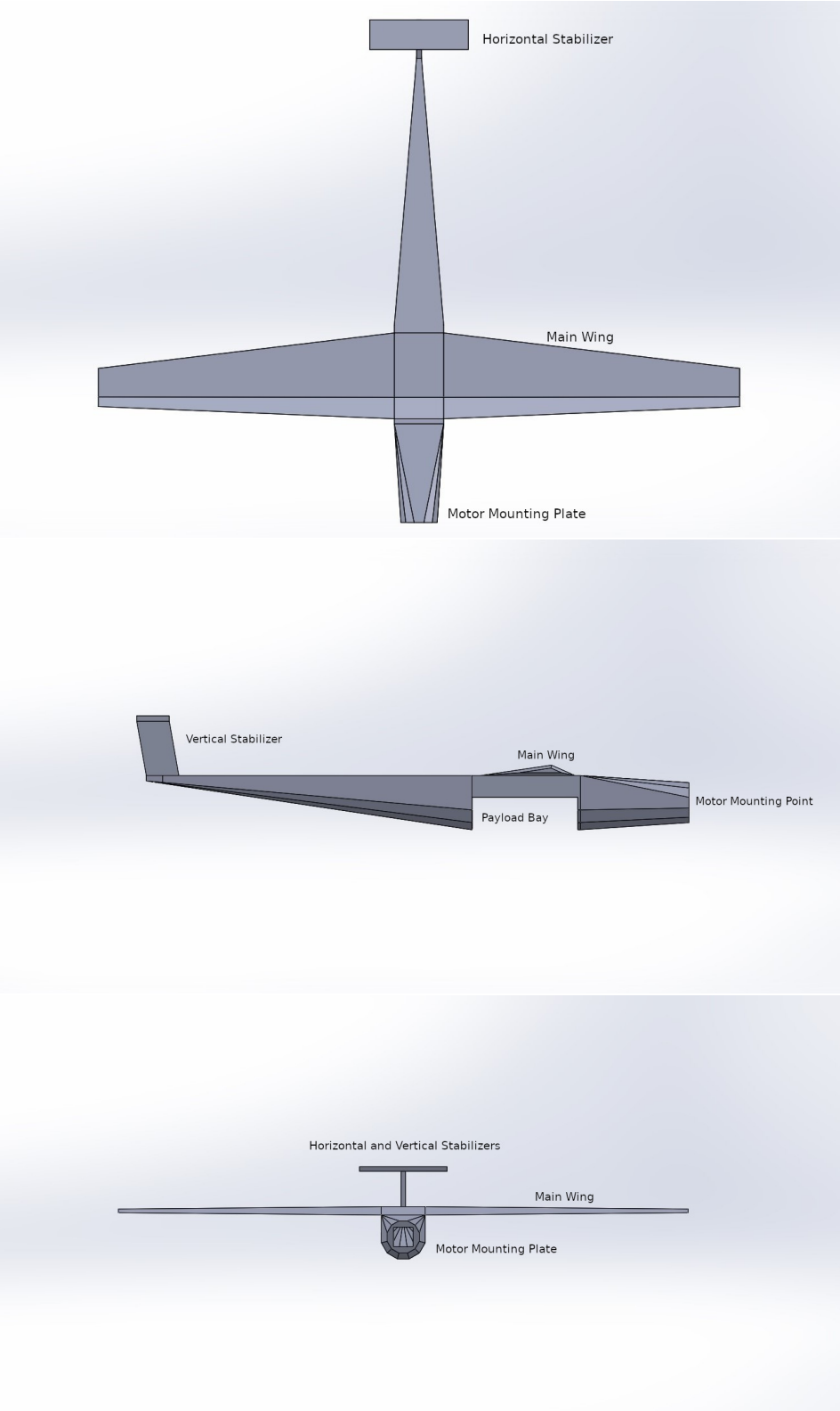

Figure 2: Three-dimensional view of final aircraft design.

Figure 3: Final aircraft construction.

1.1 Background and Literature Review

The WPI MQP design competition is a continuation of the SAE Aero design competition in which previous MQP teams participated. We therefore conducted a review of previous MQP reports to inform our design process.

In particular, we studied the 2012 MQP design team's submission, which consisted of a cranked-high-wing conventional tail aircraft. The aircraft was required to be capable of disassembly and fit within a specified volume with a limited time allotted for re-assembly. This latter constraint determined many design decisions, but does not apply to our aircraft. In particular, this constraint led the 2012 team to design a rib and film wing, as opposed to our fiberglass monocoque wing design.[14]

1.1.1 Ground Effect

Ground effect is a phenomenon wherein airfoils in close proximity to the ground experience a marked reduction in drag and an increase in lift for a given angle of attack. Ground effect has been heavily studied since the dawn of aviation due to its influence on aircraft in the takeoff and landing stages of flight.[18]

A common way of modeling ground effect is by using what is called the "mirror" technique. This involves the placing of a second, identical airfoil reflected across the "ground" line. In principle, the downwash from the main airfoil is perfectly balanced by the downwash of the mirror airfoil, such that no mass flows through the line of symmetry.[11]

For a finite wing, the presence of the ground in close proximity to the wing diminishes the effect of wingtip vorticies which are normally formed due to the difference in pressure between the upper and lower surfaces of the wing. For free stream flow, this effect is usually mitigated by having a wing with a large aspect ratio or a wingtip device.

1.2 Project Goals

The main goals of this fixed-wing MAV MQP are as follows:

- Produce a design for a fixed-wing, remote-controlled MAV that complies with the internal WPI competition rules set forth by the WPI faculty to be used in competition in spring 2020.
- Perform aerodynamic analysis of the aircraft to ensure it is capable of flight.
- Perform structural analysis to ensure the aircraft does not spontaneously disassemble in flight.
- Perform stability analysis to ensure the aircraft is statically and dynamically stable and to ensure easy operation of the aircraft.
- Select and analyze an appropriate propulsion system for the aircraft to meet aerodynamic specs.
- Construct prototypes of the MAV to use in wind tunnel and flight testing.
- Construct a final MAV design for use in the internal competition.

1.3 Project Design Requirements, Constraints, and Other Considerations

This MQP is guided by the rules for the 2020 WPI UAV Competition set forth by the faculty of the Aerospace Engineering department, displayed in full in Appendix B. These rules are comprehensive and cover subjects such as mission requirements, venue, payload and delivery, target demarcation, no-fly zones, takeoff, flight, landing and autonomy. First of all, the mission requirements are to take off from a specified area, deliver a payload at a specified target location, and land in the same area as the aircraft took off. Aircraft will be scored based on a variety of factors. A scoring analysis can be found in a later section. The venue will be at the Millis RC Club, Bill Martin Field in Medfield, Massachusetts, with the opportunity for flight tests there before the competition.

The payload is specified by the rules as taking the form of standard beanbags that must be air-dropped on the target location. These beanbags may be altered only by removing or adding sand and must be contained or fastened into a single unit to be dropped by the aircraft. The target location will have visibly distinctive markings in addition to the provided GPS coordinates and the allowance of a single identification aid, such as a QR code or beacon.

The flight rules can be split into separate categories for takeoff, cruise, and landing. For takeoff, the allowable methods are ground roll (standard takeoff), hand launch, or catapult launch. The aircraft must climb to an easily observable altitude by the end of the takeoff zone as specified at the venue. For cruise flight, the aircraft must fly at an altitude that can be easily observed by a judge in the takeoff zone to be a reasonable ground clearance or flight data must be provided to prove that this rule is met. The aircraft must also avoid the specified no-fly zones at the venue, while also remaining below a 100 meter above ground level altitude limit. For landing, the aircraft must remain within the specified landing zone throughout the entire landing process and touch-and-go landings are not allowed.

The judges will also score the autonomy of the aircraft based on the following categories:

1. Autopilot: the aircraft maintains steady flight.
2. Waypoint guidance: the aircraft travels through a sequence of spatial waypoints.
3. No-fly zone avoidance: the aircraft plans and executes maneuvers to avoid no-fly zones.
4. Target detection: the aircraft detects the target location using visibly distinctive markings.
5. Payload drop: the payload is autonomously released from the aircraft.

For these autonomy categories to be demonstrated, the pilot's hands must remain visibly out of contact with the controls for the duration of the "autonomy".

The competition rules also impose some design constraints including:

- The empty CG must be marked on the fuselage or underside of both wings.
- The gross takeoff weight must not exceed 3 kilograms.
- Aircraft must me remotely controllable at all times.
- The radio control system must be 2.4 GHz with a functional fail-safe that will kill the throttle if signal is lost.
- Spinners or safety nuts are required.
- Metal propellers are not allowed.
- Lead is prohibited in construction.
- The payload cannot contribute to the structural integrity of the aircraft.
- Ballast must be clearly indicated on drawings, be secured in flight, and not be used in the closed payload bay.
- Only electric motors are allowed to power the aircraft. No other potential energy sources are allowed other than a catapult launch.
- Control surfaces must not feature excessive slop.
- Servos must be adequately sized and backed up by analysis.
- Clevis keepers are required.
- A red arming plug must be used at 40 percent to 60 percent of the aircraft's length to arm and disarm the electric propulsion system.
- Batteries must be secured during flight and away from other protrusions that could pierce them. Batteries should be lithium polymer, with a 3 cell, 2200 mAh maximum.
- Aircraft must use a 1000 Watt power limiter.
- All team pilots must be current members of either the Academy of Model Aeronautics or the Model Aircraft Association of Canada.
- The aircraft must stay intact and not lose any pieces during flight. The only exception to this rule is a broken propeller on landing.

1.4 Project Management

This MQP consists of a team of four individuals: Marc Umbricht, Keith Blackstock, RJ Bellitto, and Conor Blomquist. The team decided on an approach that would give each team member design responsibility for one large aspect of the design process. Marc is in control of the aerodynamics of the aircraft, Keith is in control of the manufacturing and construction of the aircraft, RJ is responsible for the propulsion design and autonomy stack for the MAV, and Conor is responsible for the structural analysis and stability analysis. However, this method does not mean that the team members cannot work on other aspects of the aircraft. Throughout the project, the team collaborates on important design decisions, along with assisting any other team member that may need help. All team members participate in weekly presentations to the faculty advisors for the MQP, each providing updates relating to their specific responsibilities.

1.5 MQP Objectives, Methods, and Standards

The objectives of this MQP reflect the Project Goals outlined in Section 1.2.

- Perform aerodynamic analysis of the aircraft to ensure it is capable of flight.
  - Perform airfoil analysis in both two and three dimensions utilizing both classical aerodynamic theory and XFLR5 software.
- Perform structural analysis to ensure the aircraft does not spontaneously disassemble in flight.
  - Perform an analysis of an elliptical lift distribution using a preliminary single-spar approach followed by a stress analysis using Solidworks. Choose materials and flight specs based on these results.
- Perform stability analysis to ensure the aircraft is statically and dynamically stable and to ensure easy operation of the aircraft.
  - Utilize a series of Matlab codes and a Solidworks model to assure the dynamic and static stability of the aircraft, respectively. Use these results to assess if changes to the overall design and placement of components is necessary.
- Select and analyze an appropriate propulsion system for the aircraft to meet aerodynamic specs.
  - Choose a propulsion system in order to achieve the flight specs outlined in the aerodynamic analysis. This includes powerplant testing of various components.
- Construct prototypes of the MAV to use in wind tunnel and flight testing.
  - Decide on efficient processes and materials to construct prototypes. These preliminary constructions will provide proof that the processes chosen will work for the final MAV.
- Construct a final MAV design for use in the internal competition.
  - Utilize results from all previous analysis segments to decide on a final design. Utilize proven construction methods to fabricate a final MAV for use in the competition.

1.6 MQP Tasks and Timetable

The following Gantt charts detail the team's schedule throughout the three terms that the project was active. Specifically, they display the main objectives for each term and when work was performed on those objectives, along with their completion dates.

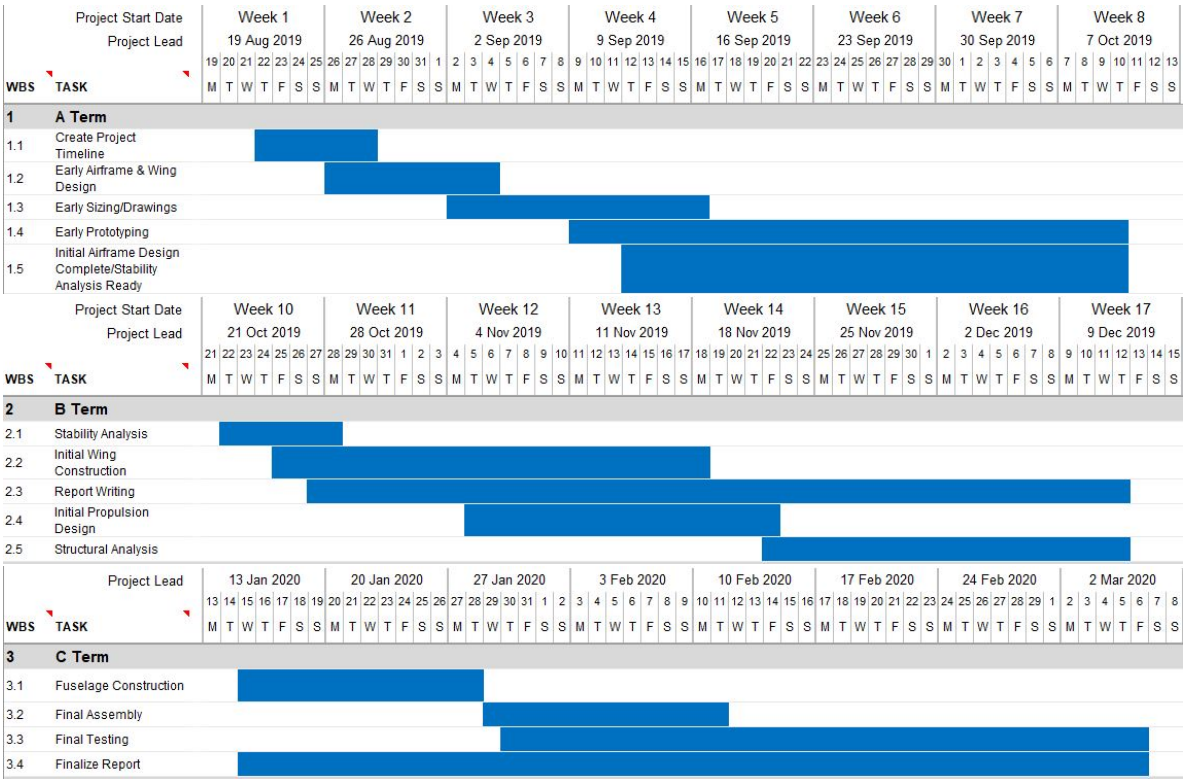

Figure 4: Gantt Chart Timeline for Fixed Wing Team 1

1.7 Final Design Parameters

The following table displays the final aircraft design parameters that were used to manufacture and test the micro-UAV at the culmination of the project. Of note are the aspect ratio of the wing, which went through many design iterations, and the final maximum payload capacity. From the payload capacity vs. the max takeoff mass, it can be seen that the final mass of the unloaded airframe was 0.985 kg.

Design Parameters	
Max Takeoff Mass	3 kg
Wing Area	0.15 m^2
Wing Loading	196 N/m^2
Wingspan	1.2 m
Mean Aerodynamic Chord	15 cm
Wing Aspect Ratio	10
Wing Taper Ratio	.43
Payload	2.015 kg
Energy Capacity	2.2 Ah
Motor	DYS D3548 790 kV Brushless
Performance	
Maximum Cruising Speed	62 m/s
Max Ragne Cruising Speed	22.1
Stall Speed	16.7 m/s
Range	52.7 km

2 Scoring Analysis

The scoring formula is given in the internal WPI competition rules as:

$$S = \lambda_1 \frac{m_{pay}}{m_{BEM}} t V_{avg} + \lambda_2 \Delta + \lambda_3 A_n + P \tag{1}$$

Where m_{pay} and m_{BEM} is the payload and basic empty masses respectively, t is flight time, V_{avg} is average groundspeed, Δ is a -1 to 1 score for hitting a ground target, A_n is a 0 to 11 point scale for automatic flight capabilities, and P is a 0 to 10 point scale for originality. The λ terms are scaling factors, where $\lambda_1 = 0.01$ and $\lambda_2 = \lambda_3 = 35$.

	Min	Max
Endurance (Λ_1)	0	358*
Bombing Accuracy (Λ_2)	-35	35
Automation (Λ_3)	0	385
Originality (P)	0	10

Table 2: Minimum and maximum scores for each scoring term.
* : The maximum score for endurance is unbounded. The values given here are assumed for a perfectly efficient powertrain, an L/D_{max} of 12, a gross mass of 3 kg, and a payload fraction of 1. This corresponds to a 35.8 km range. See **Eqn. 8**

2.1 Endurance

We can see that the second, third and fourth terms in **Equation 1** are limited to minimum and maximum values, listed in **Table 2**. The first term, however, henceforth referred to as the endurance scoring term and denoted by Λ_1, is not limited by the socring formula. It is instead limited by the energy storage of the aircraft, which is in turn limited to a three cell 2.2 Ah lithium polymer battery. The energy of an idealized battery is given by the equation:

$$E = CV \tag{2}$$

where C is the capacity and V is the voltage.[9] The voltage is directly proportional to the number of cells, and in the case of a lithium polymer battery, the nominal (ie. average) voltage per cell is 3.7 V.[9] This gives us a total energy capacity of 88 kJ.

The endurance term is a function of $t * V_{avg}$, which is equal to distance traveled by definition. The work done on the aircraft by the powertrain is equal to the product of force (in this case thrust) and distance:

$$W = Td \tag{3}$$

In cruise, the thrust is equal to the total drag. Drag at cruise is related to lift by the ratio of lift to drag at cruise velocity (L/D_{crz}). Lift is equal to weight in cruise:

$$L = mg \tag{4}$$

Thus, thrust required at cruise is given by the relation:

$$T_{crz} = \frac{mg}{L/D_{crz}} \tag{5}$$

We can then calculate the distance traveled per unit work done on the aircraft:

$$d = \frac{W \times L/D_{crz}}{mg} \tag{6}$$

Assuming that the cruise portion of flight is much longer than other phases of flight, the total work done on the airframe by the powertrain over the course of the flight can be assumed to be approximately equal to the energy capacity of the battery, modified by an overall efficiency factor η_0:

$$E = W \times \eta_0 \tag{7}$$

We can then calculate the maximum points value of Λ_1 given the critical aircraft performance parameters of L/D_{crz} and the ratio of payload mass to basic empty mass, hereby referred to as m^*:

$$\Lambda_1 = \lambda_1 m^* \frac{W \times L/D_{crz}}{mg} \eta_0 \tag{8}$$

As we can see from **Table 2**, Λ_1 can be one of the dominant scoring parameters if optimized for.

2.2 Bombing Accuracy

The scoring term for bombing accuracy, hereby referred to as Λ_2, is a 3 point stepwise function from -35 to 35. There are two scoring circles around the target; the first, considered a 'hit', has a radius of 1 m centered on the target. The second, considered a 'near-miss', has a radius of 3.5 m centered on the target. Finally, dropping the payload outside of the 3.5 m 'near-miss' circle is considered a 'miss'. The scoring formula awards 35 points for a 'hit', zero points for a 'near-miss', and deducts 35 points for a 'miss'. When compared with other scoring terms, Λ_2 is almost completely irrelevant for our design.

2.3 Automation

There is significant incentive in the scoring formula for automatic flight capability. There are five capabilities which are rewarded with differing point values, and the sum of those rewards is multiplied by $\lambda_3 = 35$. The scoring term for automation, hereby referred to as Λ_3, is given by:

$$\Lambda_3 = \lambda_3 \sum_n A_n \tag{9}$$

where A_n are the following automated capabilities:

- 3-Axis Autopilot with Altitude hold, Vertical Speed, and Indicated Airspeed modes (1 point)
- Sequential Waypoint Navigation (1 point)
- No-Fly Zone Avoidance (3 points)
- Target Identification (5 points)
- Automatic Payload Release (1 point)

Autopilot capability must be demonstrated for at least 1 minute of flight. At the airspeed we have designed for (20 m/s), our aircraft would cover 1.2 km during the demonstration. Due to the size constraints of the airfield arena, and the seriousness of a no-fly zone violation, autopilot capability necessarily requires waypoint navigation and no-fly zone avoidance in order to safely operate for the duration of the demonstration. Similarly, autopilot capability is a necessary prerequisite of waypoint navigation and no-fly zone avoidance. Therefore the first three points are essentially co-variant and can be grouped into a single "Automatic Navigation System" term worth 5 points.

Automatic payload release interestingly has the same points value as hitting the target, or conversely, equal to the points lost by missing the target completely. This means that missing the target "automatically" has no effect on scoring. Furthermore, if the automatic payload release can consistently make near-misses, it is equal in terms of points to a pilot who can consistently hit the target. It is

therefore advantageous to use automatic payload release if the system performs equal to or marginally worse than a pilot.

In reality, hitting a target from a moving aircraft is a very difficult task. In WWII, bombing was considered accurate if it hit within 100 yards of the target, using precision guidance instruments.[8] We do not believe that it can be reasonably expected of our pilot to hit the target unaided; therefore, an automated bombing computer is likely to outperform the pilot. It is therefore advantageous to us to use an automatic payload delivery system virtually regardless of its performance.

In order for a bombing computer to work, however, it needs to be able to acquire the target. Target Identification is therefore a necessary component of a bombing computer in our system, and is conveniently worth far more points than the bombing itself. At 175 points, it is the most valuable single item in the scoring formula. It is therefore one of our key design goals.

2.4 Design Optimization

The scoring analysis discussed in the previous section leads us to optimize for the following design goals:

- Endurance (approx. 360 points, limited by battery size and aircraft weight)
- Payload Fraction (modulating the points from endurance)
- Autopilot with automatic navigation (175 points)
- Automatic target detection and payload release (210 points)

The aerodynamic performance of our aircraft is a result of much more fundamental design parameters such as wing loading, aspect ratio, etc., when compared to the automation capabilities. Generic autopilot systems are commercially available and within our budget constraints which can be easily adapted to our airframe after the initial design and construction phase. Similarly, a bombing computer can be designed independently of the airframe it is used in, provided navigational data. Our initial design priority is therefore the optimization of the airframe for low-drag, high-efficiency flight.

3 Alternative Designs

We explored several alternative design concepts before settling on the current conventional T-tail design. Of paramount importance was the minimization of drag, as per our previously discussed scoring analysis. After drag performance, our second design goal was ease of operation within the competition space. Full or partial automation would be added at the end of the design process in the pursuit of this goal.

3.1 Ground Effect Vehicle

In the interest of minimizing lift, we explored the possibility of designing a ground-effect vehicle for our project. Ground effect vehicles, or GEV's, utilize the eponymous "ground effect," a phenomenon which dramatically reduces induced drag when a wing is close to the ground. Ground effect is quite complex, and can be roughly divided into three cases, strong, intermediate, and weak ground effect, delimited by height to chord ratio[11]. In the medium and weak ground effect ($h/c > 1/3$), the reduction in drag can be characterized by an increase in effective aspect ratio due to a disruption of the wingtip vorticies caused by the pressure difference between the top and bottom surfaces of the wing.[16] In this context, h is airfoil height above the ground measured from the chord line, and c is the chord length of the airfoil. The increase in effective aspect ratio is given as [16]:

$$AR_e = \frac{AR}{1-\phi}, \quad \phi = \frac{1 - 1.32(h/c)}{1.05 + 7.4(h/c)} \tag{10}$$

The competition rules severely penalize contact with the ground, which effectively disallows operation in the "strong ground effect"[11] regime, i.e. where $h/c < 1/3$. Due to the stability dynamics of reverse-delta craft, ensuring ground clearance at all times is likewise unrealistic. This leaves us with tandem wing or ekranoplan designs. For analytical simplicity, we chose to pursue an ekranoplan aircraft with an aspect ratio of 2, shown in **Figure 5**. The aspect ratio is principally limited by the ground clearance of the wingtip in a turn, which would come unacceptably close to ground contact with larger aspect ratios.

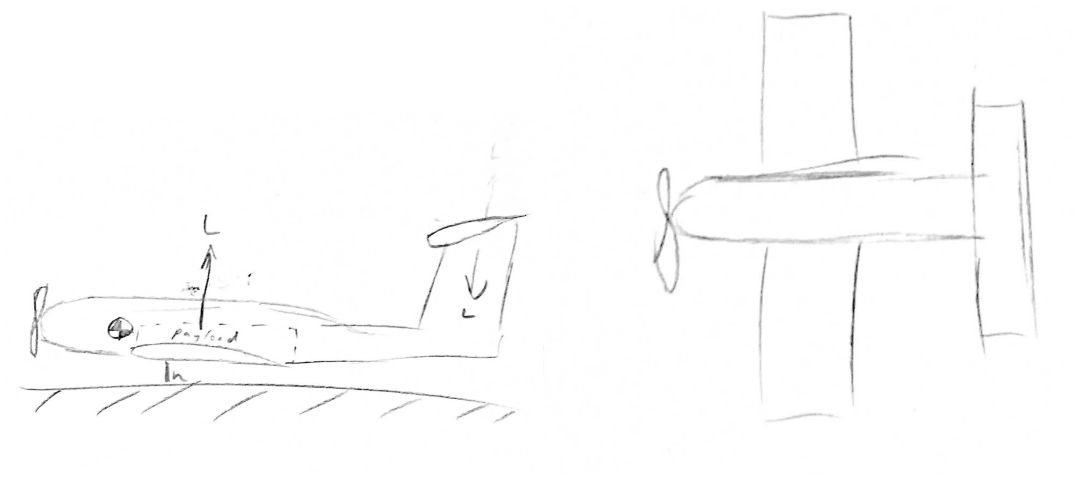

Figure 5: Preliminary design drawings for a proposed ground effect vehicle configuration.

Aside from the aerodynamic advantages of this configuration, accurate bombing would be greatly facilitated due to the short distance from the payload bay to the target. Trajectory calculation would require a greatly diminished degree of precision, and the effect of wind could be essentially neglected. In effect, lateral error could be assumed to be zero, and longitudinal error would be exclusively a function of forward airspeed.

Unfortunately, the aerodynamic advantages were estimated to be insufficient to justify the increase in operational complexity. As per **Equation 10**, the increase to our effective aspect ratio was only approximately 10%. While this would lead to a significant reduction in induced drag for a given aircraft, the advantage would be dwarfed by a motor-glider with a much larger aspect ratio.

3.2 Flying Wing Design

Commonly referred to as a "versa wing" or "flying V" Configuration, conventional flying wings benefit from a high natural structural integrity due to a more even mass distribution along the wing and a streamlined frontal profile.

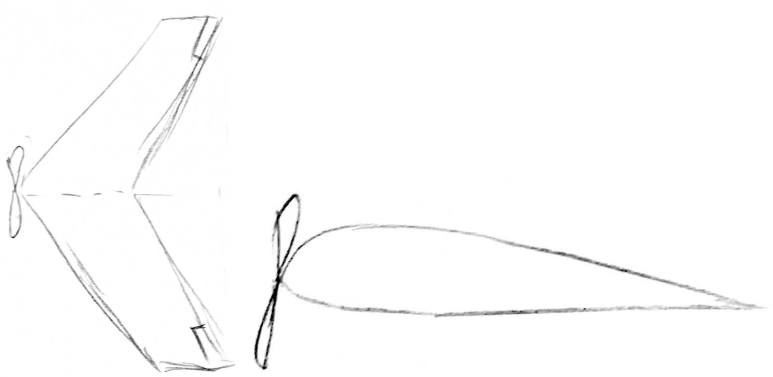

Figure 6: Preliminary design sketches for flying wing designs. The bottom figure is the optimal lift distribution in order to ensure stability in yaw.

As shown in **Figure 6**, our preliminary drawings, maintaining yaw stability without a rudder would require negative lift at the wingtips to eliminate adverse yaw.[7]

3.3 Alternative Payload Bay Designs

The design requirements of the payload bay consist of safely and securely holding the payload for the duration of flight, and releasing it at the required time with minimal delay and minimal interaction to avoid fouling the aim of the bombing computer. The simplest design which meets these requirements is an external pylon. This has significant drag contributions, however, and is therefore unsuitable for our aircraft. We therefore pursued an internal payload bay design. An early design was of a single door panel, which would be hinged at the fore of the payload bay. A servomotor would force the door open into the airflow, allowing the payload to slide out to the aft of the aircraft. Air resistance and spring pressure would then close the payload bay door. Unfortunately, this design would require a very strong servomotor, as the airstream pressure would exert a very large force on the door as it opened. It would also impart a rearward velocity to the payload, as it would slide off of the payload bay door rather than falling freely.

4 Analysis Methods

4.1 Aerodynamic Analysis

Our stated design goal is to optimize our aircraft for maximum L/D (Lift to Drag Ratio). In steady flight, lift is equal to the weight of the aircraft, and, due to our use of electric power, is therefore constant throughout the flight up until payload release. It is useful to non-dimentionalize the forces on an airfoil:

$$C_f := \frac{F}{1/2\rho v^2 S} = \frac{F}{qS} \tag{11}$$

where F is lift or drag respectively, and C_f is the non-dimensionalized coefficient of that force. ρ,v, and S are the air density, velocity, and wing reference area respectively, and $q := 1/2\rho v^2$ is the dynamic pressure. Given that lift, design cruise velocity and altitude are known, and therefore q, we can find our coefficient of lift as a function of wing area:

$$C_L = \frac{L}{qS} \tag{12}$$

Wing area is related to the wingspan b and aspect ratio AR:

$$AR := \frac{b^2}{S} \iff S = \frac{b^2}{AR} \tag{13}$$

The aspect ratio is an important parameter defining the scale of the wingspan to the total area of the wing. AR affects the relationship between the two-dimensional coefficient of lift and the actual lift coefficient of a finite wing, and has important consequences for the induced drag coefficient. A high-aspect ratio leads to a reduction of induced drag, but at the expense of increased structural reinforcement. Such reinforcement may require an increase in the thickness of the airfoil, leading to an increase in the parasite drag for an overall increase in drag. More detailed analysis of the structural limitations is discussed in the Structural Analysis section. We determined an aspect ratio of 10 to be feasible using the construction materials and techniques available to us without causing an undue constraint on the thickness of the airfoil.

4.1.1 Boundary Layer Effects

As discussed in the Literature Review section, airfoils with non-negligible thickness suffer a performance penalty in the laminar-flow boundary layer regime,[19] i.e. $Re \lesssim 5 \times 10^5$, where Re is the Reynolds Number of the flow over our airfoil:

$$Re = \frac{\rho v d}{\mu} \tag{14}$$

where here d is the chord-length of the wing and μ is the viscosity of air. For a 10 cm chord, at our airspeed of 20 m/s produces a Reynolds number of $Re \approx 1 \times 10^5$, placing our aircraft in the laminar-flow boundary layer regime.

Fortunately, a laminar flow boundary layer can be forced to transition to turbulent flow if it is 'tripped' by a surface defect larger than a critical size[15], given by the equation:

$$a_{crit} = 15\frac{\mu}{\sqrt{\tau_0 \rho^3}} \tag{15}$$

where τ_0 is the shear stress on the fluid at the surface, and can be estimated from XFLR5 simulation data.

It is beyond the scope of this project to analytically derive the optimum transition point along the airfoil. Instead, we used XFLR5, a software program which performs aerodynamic analysis based on the vortex-panel method, which can perform analysis with forced transition points. We varied the transition point along candidate airfoils in order to find the optimum location to induce a turbulent boundary layer. This transition will be induced by a wire of the dimension specified by **Equation 15** laid along the top of the wing at the optimum point.

4.1.2 Two-Dimensional Analysis

We begin our design by selecting or designing a two-dimensional airfoil, or an infinite wing, in order to avoid span-wise flow effects. We used an online database of airfoils[1] and selected candidate airfoils which had the best two-dimensional C_l/C_d ratio at low Reynolds numbers, and had a thickness greater than 10% of mean chord. Of the candidates, we were able to select the Eppler 434 airfoil,[3] which we modified by reducing the thickness to 11% of mean chord. A profile of our airfoil is shown in **Figure 7**.

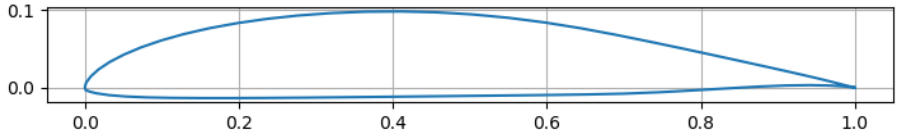

Figure 7: Our modified Eppler 434 airfoil.

Our analysis with XFLR5 showed the best performance using an upper boundary layer transition point of 50% of mean chord. XFLR5 is an analysis tool for airfoils, wings, or entire aircraft at low Reynolds numbers using the Lifiting Line Theory, Vortex Panel Method, and a three-dimensional panel method. The lift and drag curves are shown in figure 8.

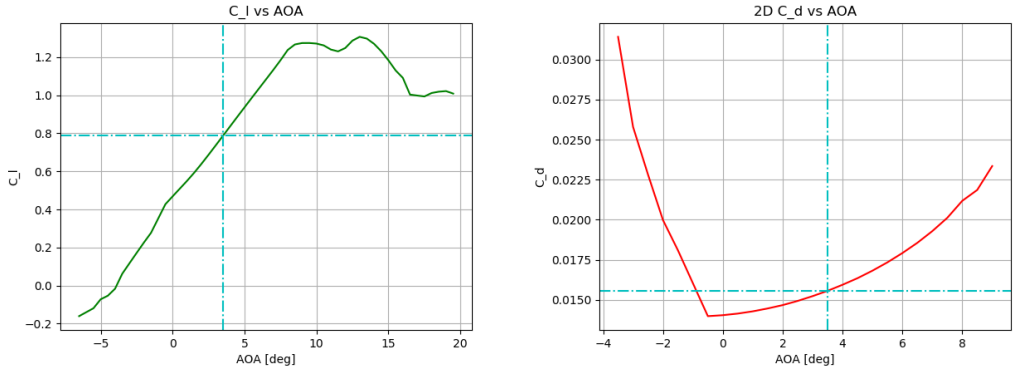

Figure 8: Two-dimensional lift and drag coefficients for our modified Eppler 434 airfoil. The cyan index is referenced to the minimum drag angle of attack found in our finite-wing analysis.

4.1.3 Finite Wing Analysis

Drag is the sum of induced drag D_i and parasite drag D_0:

$$D = D_0 + D_i, \quad C_D = C_{D0} + C_{Di} \tag{16}$$

Induced drag is generated by spanwise flow along the wing, in turn caused by the pressure differential between the top and bottom wing surfaces. For an infinite wing, air cannot flow over the wingtip and there is no spanwise flow, and therefore no induced drag. For a finite wing, induced drag is a function of the aspect ratio and the wing planform:

$$C_{Di} = \frac{C_L^2}{\pi ARe} \tag{17}$$

where e is the efficiency factor, correcting for the difference between an ideal, elliptical wing planform and the actual wing planform. In our case, we assume $e = 0.9$.

Parasite drag is a function of dynamic pressure, and therefore C_{D0} is constant. We can estimate C_{D0} by component analysis, where the total coefficient of parasite drag is assumed to be the sum of the parasite drag of each component. This is actually an underestimate of the total parasite drag, as it neglects interference drag, i.e. the interaction of the airflows around each component. The parasite drag of a component is approximated by:

$$C_{D0i} = C_{di}\frac{S_i}{S} \tag{18}$$

where C_{di} is the parasite drag coefficient of the component and S_i/S is the ratio of the reference area of the component to the reference area of the wing. Airfoil components, including the wing, vertical and horizontal stabilizers, can be computed using XFLR5, and the fuselage can be assumed to be a streamlined object with the properties $C_{df} = 0.04$ and $S_f = 0.01$ cm^2.[6]

Given these relationships, we are tasked with optimizing the wing area of our aircraft, given our design weight. We can define this in terms of our wing loading L/S, given that lift is equal to our weight of $mg = 29.4$ N. Our wing loading is optimized with the relation:

$$\frac{L}{S} = q\sqrt{\pi ARe C_{D0}} \tag{19}$$

Using our previously assumed values of $AR = 10$, $e = 0.9$, $q(20 \text{ m/s}) = 240$ Pa, and drag data from XFLR5, we perform an iterative analysis and find that our optimum wingloading is 199. This gives us a wing planform area of 0.148. From **Equation 13**, this dictates our wingspan $b = 1.22$ m. We can also now refine our coefficient of parasite drag to be:

$$C_{D0} = C_{dw} + 0.0065 \tag{20}$$

where C_{dw} is the two-dimensional drag coefficient of the wing as computed by XFLR5, and the sum of all other drag components is 0.0065.

Total Drag As shown in **Equation 16** total drag coefficient is the sum of **Equations 17** and **20**:

$$C_D(\alpha) = C_{dw}(\alpha) + 0.0065 + \frac{C_L(\alpha)^2}{\pi ARe} \tag{21}$$

As both the coefficient of lift and the coefficient of drag are functions of the angle of attack α, we can define the total coefficient of drag as a function of α. From **Equation 12** can calculate the required coefficient of lift for all values of q and thus for all values of v. The two-dimensional coefficient of lift C_l, shown in **Figure 8**, is related to the finite-wing coefficient of lift[6] C_L by the equation:

$$C_L(\alpha) = C_l(\alpha)\frac{AR}{AR + 2} \tag{22}$$

Using this relation, we can find the drag for all airspeeds. This is shown in **Figure 9**. As lift is constant, L/D is easily computed to reach 17.6 at the minimum drag airspeed, at 22 m/s.

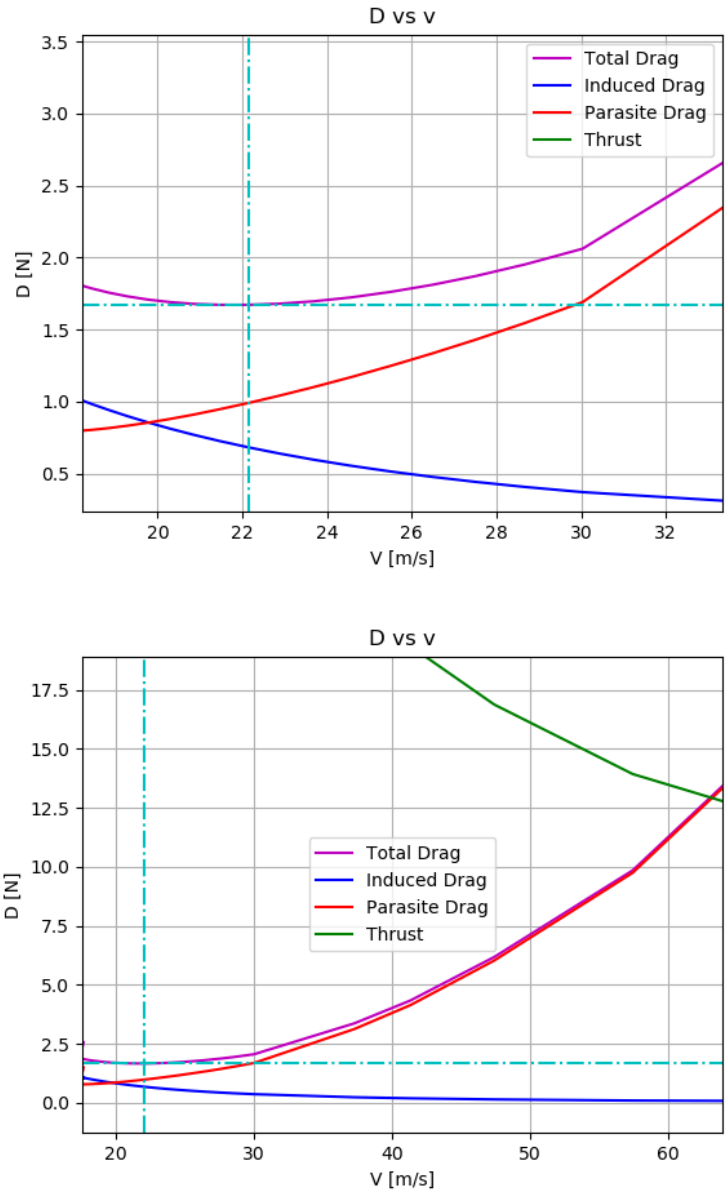

Figure 9: Total drag curve for our aircraft for the operational airspeed range of our aircraft. Max L/D is marked with the cyan index, and corresponds to a drag of 1.67 N and an L/D of 17.6, with an airspeed of 22 m/s. Notably, our MAV has considerable excess power available due to its low-drag design, providing a top cruise speed of 62 m/s.

This is notably 10% faster than the originally designed airspeed, however it remains operationally feasible to fly within the competition area. It is also important to note that the maximum L/D airspeed is at the bottom of the drag curve, i.e., it is at a point of neutral stability with respect to speed. A positive slope on the drag curve corresponds to a speed stable regime, while a negative slope corresponds to a speed unstable regime. This means that should the aircraft slow down, drag will increase, further slowing down the aircraft. Critical parameters at the cruise condition are listed in **Table 3**.

V	22 m/s
q	299 Pa
C_L	0.388
C_{D0}	0.022
L/D_{max}	17.6

Table 3: Critical parameters of our aircraft at the cruise condition.

4.2 Structural Analysis

Structural analysis is paramount in designing and constructing any aircraft to ensure the components of the aircraft do not fail during flight. This analysis was performed under the assumption of a single wing spar being the sole structural component of the wing. This spar was modeled as the fiberglass skin that was applied to the outside of the wing's foam core. Thus, the "spar" is in the shape of a hollow airfoil with the structural properties of the fiberglass, shown in figure 10.

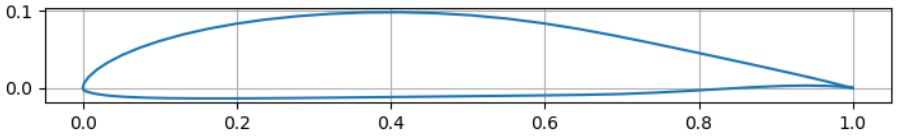

Figure 10: Fiberglass skin "spar".

The first step in this analysis was to model an elliptic lift distribution across the wingspan to simulate real flight conditions:

$$L' = L'_0\sqrt{1 - \frac{2z}{b}^2} \tag{23}$$

Where L'_0 is the lift per unit span at the wing root, z is the distance from the wing root, and b is the wingspan. The lift per unit span at the wing root can be found using the following equations:

$$\frac{nW}{2} = \int_0^{\frac{b}{2}} L'(z)dz \tag{24}$$

$$L'_0 = \frac{\frac{nW}{2}}{\int_0^{\frac{b}{2}} \sqrt{1 - \frac{4z^2}{b^2}}dz} \tag{25}$$

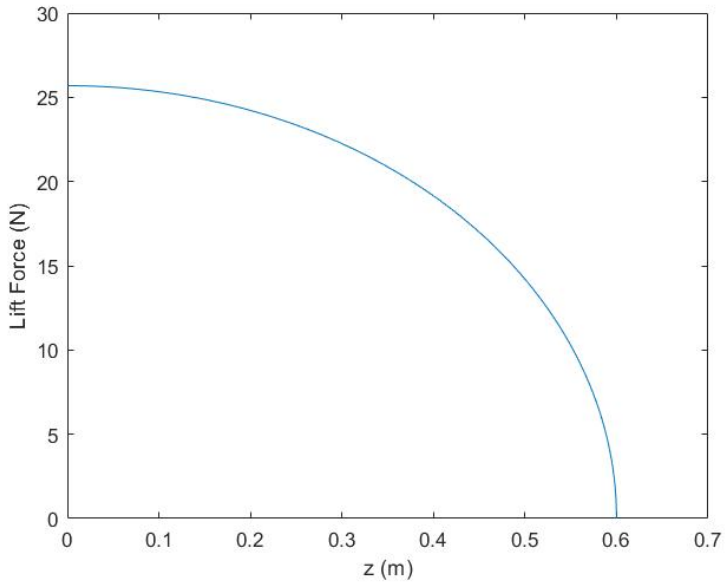

Figure 11: Example elliptical lift distribution for half span

Using these equations, and a load factor $n = 4.5$ (chosen based on a standard design load factor of 3 G's and a safety factor of 50%), the shear force throughout the entire span can be found as a function of z, the distance from the wing root:

$$V = \frac{L_0' b}{4}\left[\arcsin(\frac{2z}{b}) + \frac{1}{2}\sin\left(2\arcsin(\frac{2z}{b})\right)\right] \tag{26}$$

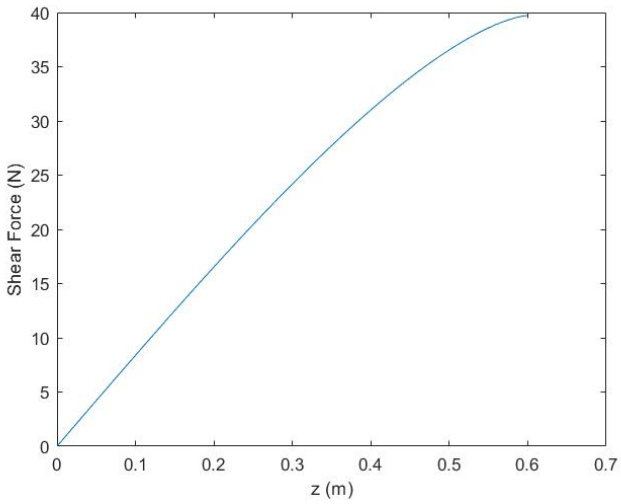

Figure 12: Theoretical shear force diagram

From here, the moment acting on the wing can also be calculated using the following equation:

$$M = \frac{L_0'}{4}\left[-\frac{bz\pi}{2} + \frac{b^2+2z^2}{3}\sqrt{1-\frac{4z^2}{b^2}} + bz\arcsin(\frac{2z}{b})\right] \tag{27}$$

Using the second moment of area calculated in a later section (4.2.2), the maximum bending stress can be calculated. This stress occurs at the wing root where it attaches to the aircraft. Here, the maximum bending moment from the previous equations is found to be $47.67Nm$. The full bending moment distribution across a half wingspan is shown in Figure 13. Using Equation 28, the bending stress at the root is found to be 0.152 GPa. This is calculated with an I computed using 5 layers of fiberglass reinforcement, as discussed later in section 4.2.2.

$$\sigma = -\frac{yM}{I} \tag{28}$$

The maximum strain allowable for failure in a fiberglass reinforced composite is historically 1.2%.

$$\epsilon = \frac{\sigma}{E} \tag{29}$$

Using equation 29 and the calculated Young's Modulus of 18 GPa, it is found that the maximum strain at the wing root (the point of maximum stress) is 0.0085 or 0.85%. Therefore, the conclusion is that the wing structure will not fail in flight. This is, however, a single spar approximation and more in-depth calculations would be more accurate in determining the structural capabilities of the fiberglass composite wing.

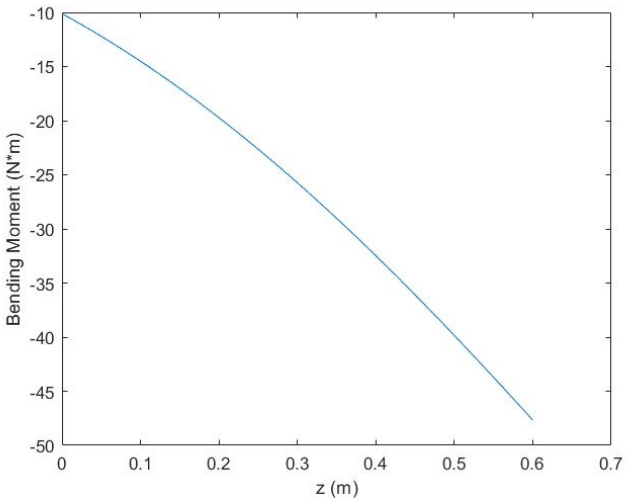

Figure 13: Theoretical bending moment diagram

4.2.1 2nd Moment of Area for an Airfoil of Known Thickness

A few of the values used in the calculations in the previous section required additional work, specifically the second moment of area for an irregular shape such as our airfoil, and the Young's modulus of a fiberglass reinforcement. As the structural makeup of our wing is primarily fiberglass reinforcement along the skin, calculating I_{xx} is non-trivial. We used a numerical method to approximate the second moment of area for a shell of given thickness around an airfoil described by a series of x-y coordinates. The code is listed in appendix A. In this section, we will describe the second moment of area in these coordinates (i.e. with x along the chord line), and therefore we will refer to $I_{yy,wing}$ in our calculations.

We first create a series of parallelograms described by the lines given by the airfoil coordinates and parallel lines shifted in the y-direction such that the thickness of the parallelogram (in the direction perpendicular to the line sections) is of the given thickness t. The distance of the displacement in the y-direction (and thus the length of the two joining lines) is found via trigonometry:

$$\Delta y = t \cos\left(\arctan(dy/dx)\right) \tag{30}$$

where dy/dx is the slope of the airfoil section. These parallelograms are then integrated over[10] with the equation:

$$I_{yy,i} = \frac{1}{12} \sum_j (x_{i,j} y_{i,j+1} - x_{i,j+1} y_{i,j})(y_{i,j}^2 + y_{i,j} y_{i,j+1} + y_{i,j+1}^2) \tag{31}$$

The total second moment of area is then the sum of each of these sections:

$$I_{yy,wing} = \sum_i I_{yy,i} \tag{32}$$

We can then scale the size of the airfoil by the chord length and perform the calculation along the entire length of the wing to find I_{xx} as a function of the position along the span of the wing.

4.2.2 Estimation of Young's Modulus of a Fiberglass Reinforced Composite

We have decided to use a fiberglass reinforced epoxy composite for our major structural components, and in order to properly model the strain and failure of these components we must model their material properties.

E E-glass Fiber	72 GPa
E Epoxy Matrix	3.5 GPa
E_l unidirectional GFRP with grain	31 GPa
E_t unidirectional GFRP cross grain	5.7 GPa
E_x GFRP in warp	18 GPa
E_y GFRP in weft	18 GPa
Lamina Thickness t	76 µm

Table 4: Material Properties of the constituent parts of our Glass Fiber Reinforced Epoxy Composite[5][4], and the approximate properties of the resultant composite assuming a 40% fiber volume fraction.

Our fiber reinforcement is a 4H satin weave. Woven fiber composites are characterized by the 'warp' (x-direction) and 'weft' (y-direction) yarns per meter, i.e. the number of transitions from the top to the bottom of the weave in the characteristic directions of the fabric. The Young's modulus given by:

$$E_x = E_y = kE_l + (1-k)E_t, \tag{33}$$

where k is given by:

$$k = \frac{n_x}{n_x + n_y} \tag{34}$$

where n_x and n_y are the yarns per meter in the warp and weft directions. The fiberglass we used had an n_x range of 190 to 203, and an n_y range of 183 to 197. This works out to a minimum k value of 0.49. The constants E_l and E_t in **Equation 33** are the transverse and longitudinal moduli of a unidirectional fiber reinforced composite[12]:

$$E_l = V_m E_m + V_f E_f, \quad E_t = \frac{E_m E_f}{V_m E_f + V_f E_m} \tag{35}$$

where V_m and V_f are the volume matrix and fiber fractions respectively, and E_m and E_f are their Young's Moduli. Using these equations, and the industry values listed in **Table 4**, we find our Young's Moduli to be 18 GPa.

4.2.3 Fuselage Structure

We used a primarily monocoque composite structure for our fuselage. This was constructed using a foam-board panel construction which was planned to be laid up with fiberglass reinforcement.The large void in the structure caused by the payload bay results in a dramatic weakening of the overall structure, particularly with respect to its longitudinal rigidity. This section of the fuselage was reinforced by a balsa wood truss structure which was designed to resist the bending moment about this section of the fuselage. In practice, it was found that the foam board panelling with the truss reinforcement was sufficiently rigid for the loads expected in flight. The structure was therefore not reinforced with fiberglass.

The payload bay doors are supported by a piano hinge, which is in turn supported in simple tension by the walls of the payload bay. By ensuring that the tension loading from the payload would be entirely supported by the foam-board walls, we were able to reduce the weight and complexity of the truss which could be designed to support a smaller tensile load.

The required load of the fiberglass walls is equal to our maximum payload (2 kg) multiplied by our maximum load factor (4.5 G), for a total load of 88.2 N. The stress applied is thus given by the equation:

$$\sigma = \frac{F}{A} \tag{36}$$

where F is the load, and A is the cross-sectional area of the fiberglass wall, in our case equal to twice the length of the payload bay multiplied by the total thickness of the laminate, itself a multiple of the lamina thickness t listed in **Table 4**.

The stress-strain relationship in simple tension is given by the equation:

$$\epsilon = \frac{\sigma}{E} \tag{37}$$

By aligning the warp direction of the fabric with the tensile load, and setting $\epsilon = 0.012$, we can solve for the required thickness of the fiberglass wall laminate:

$$nt \geq \frac{F}{2lE\epsilon} \tag{38}$$

where l is the payload bay length, 20 cm. This gives us a required thickness of 1.02 µm, less than the thickness of a single lamina. It was therefore determined that the reinforcement was unnecessary.

4.3 Power Analysis

4.3.1 Battery Analysis

Electric propulsion is most favorable when aircraft reach certain smaller sizes, such as MAV's, or when there are other mission requirements such as stealth.[17]. As discussed in the introduction, the battery for this aircraft is limited to a 2200 mAh 3-cell lithium polymer battery to power the MAV. In the design and construction of any battery powered aircraft, the questions of range and endurance are first and foremost. Using the battery hour rating Rt, the total efficiency of the entire propulsion system (including motor and propeller) η_{tot}, the capacity of the battery C, the voltage of the battery V, the wing area S, the weight of the aircraft W, and the parasitic drag coefficient C_{D0}, Traub derived the following equations to estimate both the range and endurance time of a battery powered aircraft.

$$E_{max} = Rt^{1-n}\left(\frac{\eta_{tot}VC}{C_{D0}^{\frac{1}{4}}\frac{2}{\sqrt{S\rho}}(2W\sqrt{\frac{k}{3}})^{\frac{3}{2}}}\right)^{n} \tag{39}$$

$$R_{max} = Rt^{1-n}\left(\frac{\eta_{tot}VC}{C_{D0}^{\frac{1}{4}}\frac{1}{\sqrt{S\rho}}(2W\sqrt{k})^{\frac{3}{2}}}\right)^{n}\sqrt{\frac{2W}{S\rho}\sqrt{\frac{k}{C_{D0}}}} \tag{40}$$

Using these equations, where $n = 1$ since it is a brand new battery and using an assumed total efficiency of 0.6 (until wind tunnel testing is performed to calculate actual total efficiency), the battery-limited maximum range of the aircraft is 39.5 kilometers and the maximum endurance is 7.4 hours. Note that these numbers are just estimates and are based solely off of the assumption that the battery is powering only the motor and electronic speed controller. In the actual competition and realistic flight, the battery will also be powering the autopilot system along with any other electronics such as an onboard computer. This will result in more power draw than these equations anticipate, lowering the maximum endurance and range. However, the team finds that the maximum range is significant enough that any auxiliary power draw from the battery will keep the range well within acceptable parameters.

4.3.2 Propulsion System Design

Due to the competitive restriction of a 2200mAh battery, much consideration had to be allocated for power consumption. Coinciding with the project goals, an optimal flight time would have to be achieved through a balance of the aerodynamic properties of the craft and power draw from the motor and control systems, with both related against the constant value of our gross liftoff weight (GLOW). In the interest of introducing a dependable margin of error, a GLOW of the maximum allowed value (3 kg) was assumed.

Component selection for propulsion systems involves a cross-sectional analysis between a provided battery type and electronic speed controller (ESC). The prop size and pitch can then be adjusted to maximize the output efficiency of a provided motor. In order to determine our optimal build, the web interface, propCalc, was utilized with our known values. Use of a 2200mAh battery running with 3 cells in series was implemented as a constant, with a 30A ESC chosen as a non-constant test variable. ESC amperage ratings are conclusively determined in accordance with the motor type, and as this had yet to be confirmed, this test variable was based on its recommended electric potential range of 7.4-14.8V. Our power source, a Turnigy lithium polymer battery with 3 cells in series, falls within this range at 11.1V.

With tentative known variables acquired, several variations of prop configuration and motor types were plugged in to achieve a load within the battery's constraint of a 25 C efficiency rating. The propCalc interface keeps a record of common, commercially available motors and their respective performance data for use in determining the potential efficiency of an aircraft. Therefore, a specific unit could be chosen for purchase from these simulations with a negligible margin of error from the presented expectations. Ultimately, a DYS D3548 outrunner motor capable of a 790 Kv frequency and a max load of 1.8A was chosen in conjunction with a 10 in. twin prop with a 6 in. pitch. This was able to stay well under our 1000W limitation, sitting at only a 176.7W power consumption and leaving a large breadth for control system load. A C rating of 7.59 was also achieved, placing it sufficiently within the battery's capabilities. Outrunner motors have the advantage of being able to radiate away heat at a fast rate, with our simulations estimating an internal temperature of only a 7 degrees Celsius. Considering the external mounting of the motor, high thermal efficiency was expected, with a lack of waste heat contributing to its low power consumption.

4.4 Stability Analysis

The stability of an aircraft is paramount to its ability to fly without major input from a pilot. For this project it is even more important since there will be a period of autonomous flight in the final competition. There are two types of aircraft stability: Static stability and Dynamic stability. Static stability is the tendency of the aircraft to return to its trim condition when met with a pitch disturbance and is based on the location of the center of gravity, while dynamic stability is described as the tendency of an aircraft to, when disturbed, return to its original state while damping oscillations caused by the restorative moments and is based on aircraft geometry and sizing.

4.4.1 Static Stability

Static stability is described as the tendency of an aircraft to return to its original position and orientation after a pitch disturbance. An aircraft is statically stable if the pitching moment returns the aircraft to trim conditions, statically neutral if the pitch disturbance is uncorrected but does not worsen, and statically unstable if the pitching moment adds to the pitch disturbance, flipping the aircraft. The static stability of the aircraft is dependent on a few aircraft characteristics, mainly the position of the center of gravity and the location of the neutral point.

In order to determine the center of gravity of the aircraft, a three-dimensional model was constructed using Solidworks, shown previously in Figure 1 where the software would automatically calculate the location of the center of gravity in relation to the nose of the aircraft. However, this center of gravity is slightly inaccurate because the heavier components such as the motor, ESC, autopilot, and battery have not been modeled yet. Thus, the center of gravity is actually farther forward than the one shown in the Solidworks model. Finding the location of the neutral point involves calculating the location on the aircraft where the derivative of the pitching moment with respect to angle of attack becomes zero. The condition for positive static stability is the following: the center of gravity must be forward of the neutral point. The following equations show the process of calculating the neutral point, including calculation of lift curve slopes for the wing and tail, the tail volume coefficient, and the downwash derivative:

$$a_{wb} = \frac{2\pi(AR)}{2 + \sqrt{\frac{(AR)^2(1-M^2)}{k^2}(1 + \frac{\tan^2(\Lambda)}{(1-M^2)}) + 4}} \tag{41}$$

where

$$k = \begin{cases} 1 + \frac{(AR)(1.87-2.33x10^{-4}}{100} & (AR) < 4 \\ 1 + \frac{8.2-2.3\Lambda-(AR)(0.22-0.153\Lambda)}{100} & (AR) \geq 4 \end{cases}$$

$$\frac{\partial\epsilon}{\partial\alpha} = 4.44\sqrt{1-M^2}\left[(\frac{1}{(AR)} - \frac{1}{1+(AR)^{1.7}})(\frac{10-3\lambda}{7})(\frac{1-\frac{\bar{l}_{tv}}{b}}{\frac{2\bar{l}_t}{b}^2})\sqrt{\cos\Lambda}\right]^{1.19} \tag{42}$$

where $\bar{l}_t$ and $\bar{l}_{tv}$ are the distances from the aerodynamic center of the wing (quarter-chord point) and the aerodynamic centers of the horizontal and vertical tails, respectively.

$$\bar{a} = a_{wb}[1 + \frac{a_t}{a_{wb}}\frac{S_t}{S}(1 - \frac{\partial\epsilon}{\partial\alpha})] \tag{43}$$

where a_t is calculated the same way as the wing lift curve slope a_{wb}.

$$\bar{V}_H = \frac{\bar{l}_t S_t}{\bar{c}S} \tag{44}$$

And finally:

$$h_n = h_{nwb} + \frac{a_t}{\bar{a}}\bar{V}_H(1 - \frac{\partial\epsilon}{\partial\alpha}) \tag{45}$$

where the neutral point is located a distance $h_n\bar{c}$ behind the leading edge of the wing. Figure 14 below shows the calculated neutral point in relation to the loaded center of gravity. The loaded CG was determined empirically rather than calculated, as an empirical process proved significantly quicker and easier. Obviously, the loaded center of gravity is much farther ahead of the neutral point than expected. Thus, if the aircraft is to achieve a static margin of 15%, ballast must be used to move the center of gravity farther backwards towards the trailing edge of the wing. The current static margin is within $85-90\%$. Without ballast, the aircraft is statically stable, but possible too much so, meaning it would be sluggish in flight. This is because with a high static margin, the horizontal tail surface must be designed to overcome a larger moment from the wing lift force, leaving less tail area for control surfaces. This hurts the aircraft's ability to maneuver quickly.

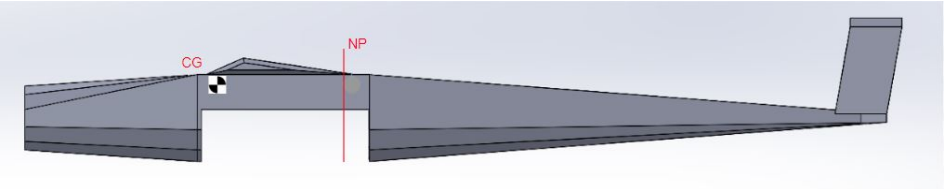

Figure 14: Location of Neutral Point w.r.t. CG

4.4.2 Dynamic Stability

The dynamic stability of the aircraft is described as the tendency of an aircraft to, when disturbed, return to its equilibrium, or trim state. An aircraft that is neutrally dynamically stable will not return to its original state, but the oscillations caused by restorative moments will maintain the same amplitude. An aircraft with positive dynamic stability will damp the oscillations and return to its original state or close to it without pilot input, with control inputs significantly reducing the time to do so. A negatively dynamically stable aircraft will have the opposite behavior - the oscillations will steadily grow larger and larger until the aircraft is impossible to control. In this case the calculations were performed for longitudinal dynamic stability to determine if the current aircraft is positively dynamically stable.

In order to assess the longitudinal dynamic stability of the aircraft, there are a collection of both non-dimensional and dimensional stability derivatives that must be calculated based on trim conditions and aircraft geometry. These derivatives were all calculated using Matlab, shown in Appendix A. An example equation for one of these derivatives is shown in equation 47, however there are too many to effectively list them all here. After these stability derivatives were obtained, they were compiled into the following longitudinal stability matrix as follows:

$$A_{long} = \begin{bmatrix} \frac{X_u}{m} & \frac{X_w}{m} & 0 & -g\cos\theta_0 \\ \frac{Z_u}{m-Z_{\dot{w}}} & \frac{Z_w}{m-Z_{\dot{w}}} & \frac{Z_q+\mu_0}{m-Z_{\dot{w}}} & \frac{-mg\sin\theta_0}{m-Z_{\dot{w}}} \\ \frac{1}{I_y}[M_u + \frac{M_{\dot{w}}Z_u}{m-Z_{\dot{w}}}] & \frac{1}{I_y}[M_w + \frac{M_{\dot{w}}Z_w}{m-Z_{\dot{w}}}] & \frac{1}{I_y}[M_q + \frac{M_{\dot{w}}(Z_q+\mu_0)}{m-Z_{\dot{w}}}] & -\frac{M_{\dot{w}}mg\sin\theta_0}{I_y(m-Z_{\dot{w}})} \\ 0 & 0 & 1 & 0 \end{bmatrix} \tag{46}$$

$$X_u = -2\frac{mg}{V^*}\sin\theta^* - \frac{1}{2}\rho^* V^* S(C_{D_u} + 2C_D^*) \tag{47}$$

From this stability matrix, the next step is to calculate the eigenvalues. If the eigenvalues all have negative real parts, then the aircraft is longitudinally dynamically stable. The eigenvalues for this aircraft are as follows:

-3.8432 + 8.6719i
-3.8432 - 8.6719i
-0.0059 + 0.8991i
-0.0059 - 0.8991i

From this result, it is obvious that the aircraft is longitudinally dynamically stable, since all of the eigenvalues of the longitudinal A matrix have negative real parts. The figures below are plots from Matlab showing the damped responses to various disturbances in pitch angle, angle of attack, and airspeed. Note that these plot the disturbance from the trim value over time, not the actual value of the parameter. These responses are properly damped, as the amplitude of the oscillations decreases with time, eventually returning to the trim values. Some control design would be able to decrease the time with which the responses return to trim values as well.

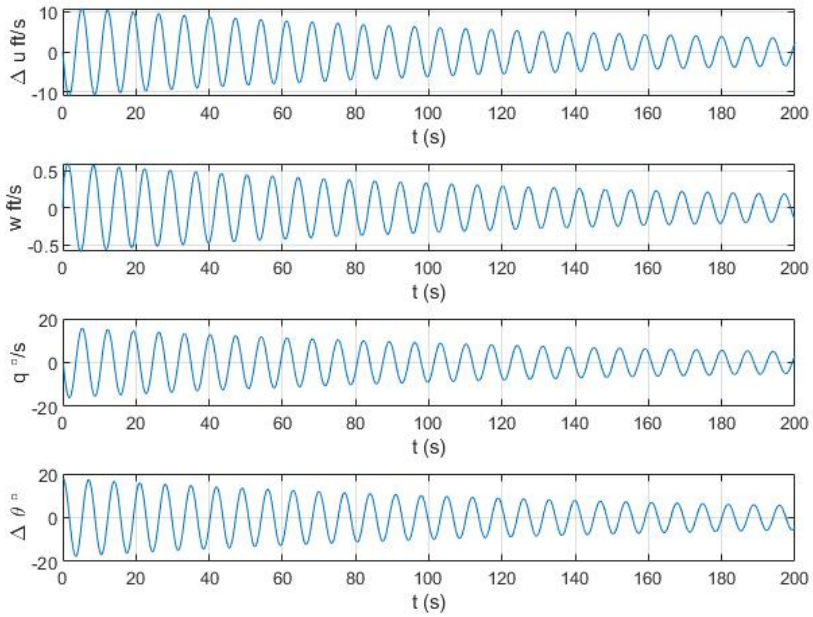

Figure 15: Response to Pitch Disturbance

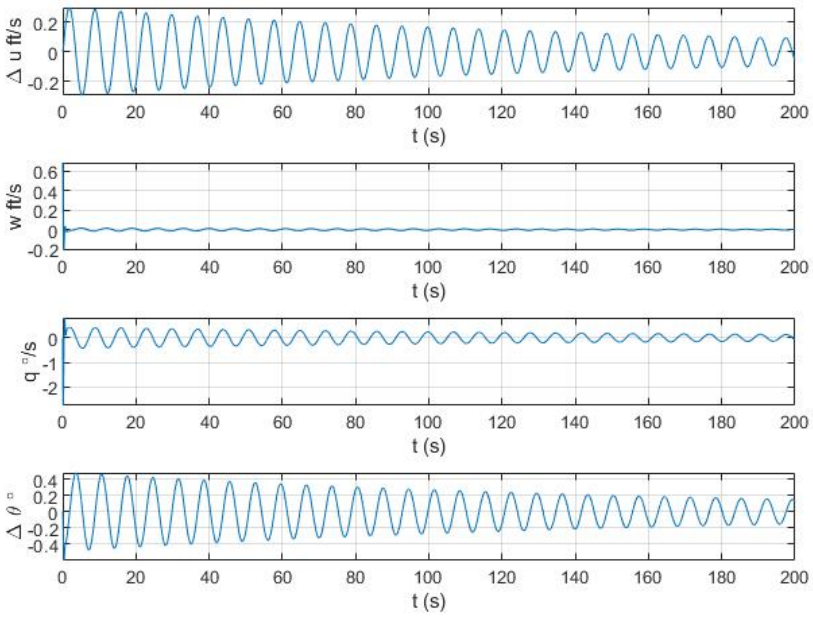

Figure 16: Response to Angle of Attack Disturbance

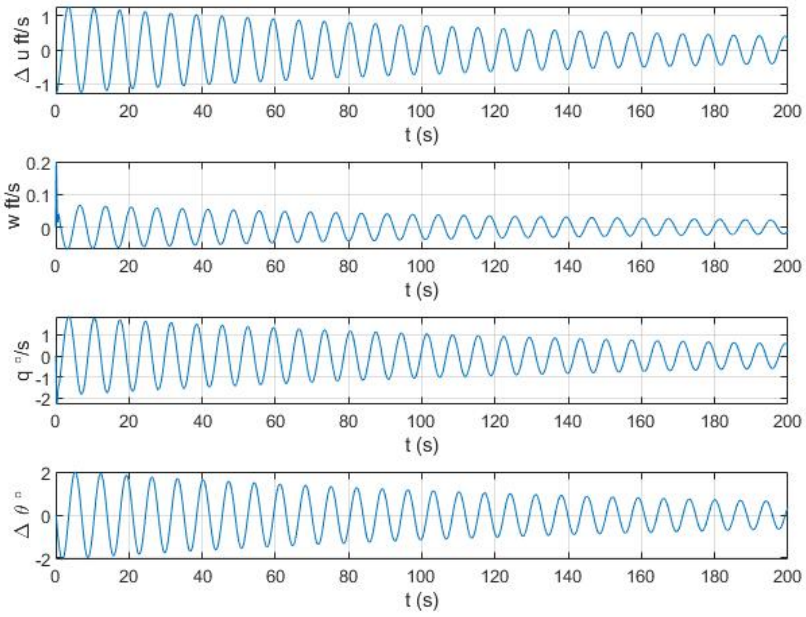

Figure 17: Response to Airspeed Disturbance

4.5 Landing Gear Analysis

An aircraft that wishes to terminate its flight without damage requires a mechanism to absorb the shock of touchdown and to safely decelerate from flight speed to a complete stop. Our aircraft is no exception, and we have elected to use a 'retractable,' conventional landing gear using a simple leaf-spring suspension shown in **18**, due to an unacceptably high drag contribution from external landing gear.

4.5.1 Fixed-Gear Drag Analysis

According to literature, the $C_{D\pi}$ of a tire and leaf-spring are 0.25 and 1.4 respectively.[13] Using the dimensions shown in **Figure 18**, we find that the frontal area for the tire and the leaf spring are 76 mm^2 and 254 mm^2 respectively. We find the 'Drag Area'[13] D/q using the equation:

$$D/q = C_{D\pi} A_{front} \tag{48}$$

Drag Area is related to the component parasitic drag coefficient $C_{D0,gear}$ by multiplying the sum of the D/q's by 1.2 to account for interference drag, and then dividing by the wing reference area S, which is 0.15 m^2. This gives us a total parasitic drag due to landing gear of $C_{D0,gear} = 0.0069$. At cruise, this results in an increase in parasite drag of approximately 31%. It is also greater than the total drag due to the fuselage, and is therefore unacceptable for our design.

4.5.2 Gear Sizing and Loading

As a result of the drag analysis in the previous section, the landing gear of our aircraft is stowed in the payload bay, and is limited by the dimensions of that space. In order to guarantee clearance, we have limited the stowed length of the landing gear to 15 cm. By adding a hinge to the middle of the

landing gear main strut, we are able to double the deployed length of the landing gear to 30 cm. The deployed dimensions of the landing gear system are shown in **Figure 18**.

We designed the gear system to maintain 10 cm of propeller clearance in the unloaded position, assuming a level attitude. In order to ensure propeller clearance on touchdown, we must calculate the total landing gear deflection on landing. This in turn requires us to estimate the vertical speed, or 'Sink Rate' V_{sink} at touchdown. Most commercial and general aviation aircraft are rated for a sink rate of 3 m/s. This is excessive for an aircraft of our scale. We therefore estimate the worst case sink rate to be maintaining a 3-degree descent at cruise velocity all the way to touchdown. Ordinarily this would be a grossly incompetent display of piloting skill, as a normal landing procedure involves a 'flare' to arrest sink rate just before touchdown. We are therefore confident that it is a reasonable upper bound for our analysis. V_{sink} can be then found using simple trigonometry:

$$V_{sink} = V_{crz} \sin(\theta) \tag{49}$$

This gives us a maximum sink rate of 1.2 m/s.

The total landing gear deflection[13], or 'Stroke' dy, is given by the equation:

$$dy = \frac{V_{sink}^2}{2g\eta_{gear}N_{gear}} \tag{50}$$

where η_{gear} is the shock absorbing efficiency of the landing gear (0.5 for a solid spring[13]), and N_{gear} the gear load factor, a measure of the load transferred to the aircraft fuselage, given by **Equation 51**[13]:

$$N_{gear} = \bar{F}_{gear}/W_{land} \tag{51}$$

where $\bar{F}_{gear}$ is the average load on the landing gear, and W_{land} is the weight of the aircraft at touchdown. In our case, we assume the maximum landing mass to be 1.5 kg, and therefore the max landing weight to be 14.7 N.

As we know that our maximum deflection is limited to 10 cm, we can derive N_{gear} from **Equations 50 and 51**, adding a safety margin of 2 cm to avoid prop strike:

$$N_{gear} = \frac{V_{sink}^2}{2g\eta_{gear}dy} \tag{52}$$

This gives us an N_{gear} of 1.9, meaning that a total of 27.9 N are transferred to the fuselage. This is well within the structural tolerances of the airframe. The required rigidity of the landing gear is

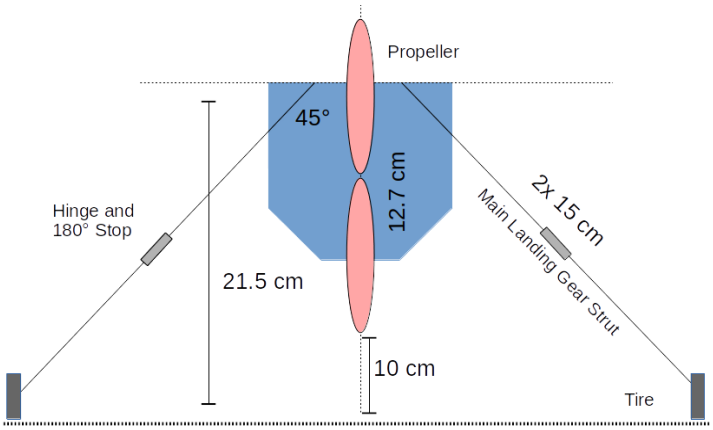

Figure 18: A schematic diagram of the landing gear system in its fully deployed configuration.

derived[13] from the equation:

$$dy = W_{land} N_{gear} \sin^2(\theta) \frac{l^3}{3EI} \tag{53}$$

where l is the length of the landing gear strut (30 cm), E is the Young's Modulus and I is the second moment of area of the strut. θ is the mounting angle of the landing gear strut, in our case 45°as shown in **Figure 18**. As we are using rectangular aluminum beams, the Young's Modulus is 69 GPa[2], and I is given by the equation:

$$I = \frac{bt^3}{12} \tag{54}$$

where b is the width and t is the thickness of the beam. Solving **Equation 53** for I:

$$I = W_{land} N_{gear} \sin^2(\theta) \frac{l^3}{3Edy} \tag{55}$$

This gives us a required I of 22.8×10^{-12} m^4. Dividing this value in half to represent the contribution of both landing gear struts, we find we need each strut to have an I of 11.4×10^{-12} m^4. This is slightly less than the I of $1/2 \times 1/8$ inch dimensional aluminum stock, which we have selected as a landing gear material.

4.5.3 Gear Deployment Mechanism

The landing gear begins in the stowed position, as it is unnecessary for the catapult launch system. It is folded in the payload bay, above the payload as shown in **Figure 18**. The payload bay doors press the payload against the landing gear, compressing the deployment springs. Upon payload release, the payload falls away and torsion springs mounted on the strut hinges bring the landing gear into the fully deployed position, where it remains for the remainder of the flight as shown in **Figure 18**.

This system provides nearly as much simplicity as a fixed gear system, while gaining the aerodynamic benefits of a retractable gear system. It does, however introduce three severe operational limitations: First, the landing gear cannot be deployed without releasing the payload. Second, the landing gear cannot be retracted after deployment. Finally, payload release must occur simultaneously with gear deployment. We evaluate these limitations to have negligible impact on the design mission,

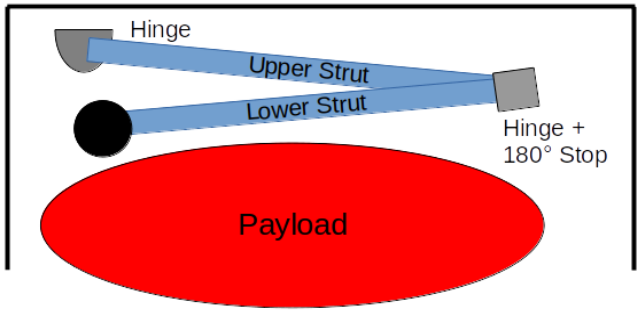

Figure 19: A Schematic of the landing gear in the retracted position. The payload compresses the landing gear deployment springs which are housed in the hinges.

as payload release happens immediately prior to landing. There is therefore no significant ferry leg after payload release, during which significant drag losses would occur. Furthermore, the payload is non-hazardous, meaning that release outside of the target zone does not pose a danger to people or infrastructure on the ground.

4.6 Fabrication

In this section, the fabrication methods for the aircraft are described. The Javelin fuselage – from front to back – can be considered as three distinct sections; the cockpit, the cabin, and the tail, each of which house specific components.

The cockpit houses the engine mount, ESC (electronic speed controller), receiver, and Pixhawk autonomous control unit (discussed in further detail in 4.3). The cabin comprises the payload bay and payload release mechanism. The tail contains the two servo motors responsible for articulating the rudder – with the elevator servo nestled in the vertical stabilizer.

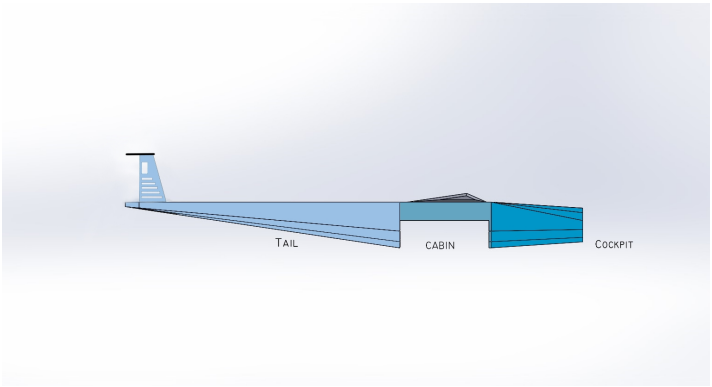

Figure 20: Fuselage

If one were to slice, separate, and flatten the cockpit and tail sections illustrated above, they would observe the following folding-scheme. Along the inner lines, a wedged channel of about 90 degrees is routed by hand with a razor blade, so as to accommodate folding.

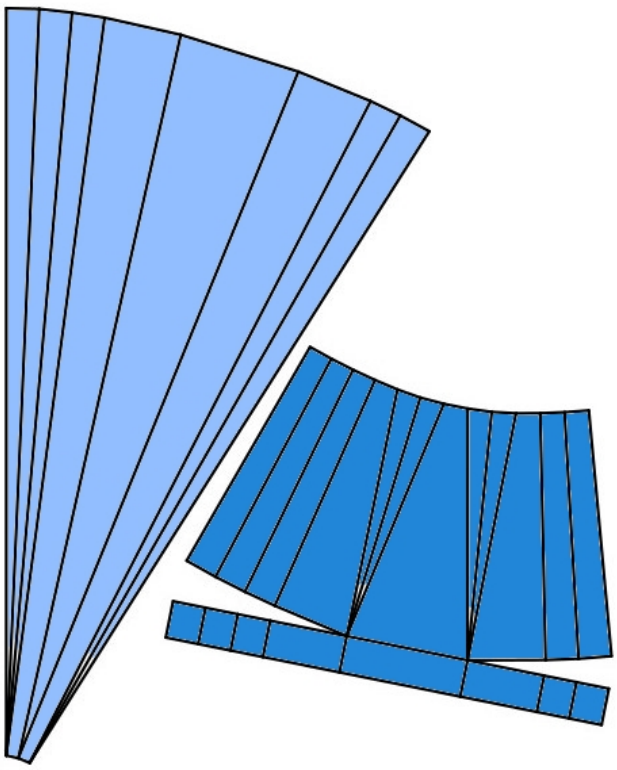

Figure 21: Folding Patterns

Once folded, these pieces (along with the cabin) are then adhered to one another via hot glue. The balsa-wood cabin truss doubles as an internal mechanical linkage between the three sections, as the upper frame extends an extra inch in both directions. In the beginning of C-term we managed to configure a laser-cutting profile for the fuselage air-frame. In the event of a destructive crash — which happened — we would be able to quickly score, fold, and assemble these precise cutouts for rapid reconstruction.

Figure 22: Power-Pod Assembly

The entire fuselage could be characterized as a rigid-panel origami. Composed primarily of folded quarter-inch foam board, with various internal supports. Form-drag reduction, rapid construction, and internal capacity were among the chief ideas driving this concept.

A hot-wire bow cutter guided between two laser-cut wooden foils was used to shave a block of XPS (expanded polystyrene) insulation foam into our main wing. 4oz satin-weaved fibreglass was vacuum bagged onto the wing to provide tensile reinforcement. The rest of the plane's body consisted of 1/4" Foam core poster-board razor assembly.Expediency is the real benefit here. By cutting and assembling arrangements of flat segments, one can create surprisingly strong structures for the required effort. A TinkerCad profile was created to house the myriad iteration of the stabilizer, elevator, cockpit plate and internal housings. The rudder and elevator control surfaces are articulated via two 9 gram servos, one located mid-tail, and the other nestled inside the stabilizer mast. 0.5 millimeter gauge piano wire serve as the push/pull linkages on both of these surfaces.

The internals consisted of a rectangular foam-core ESC (electronic speed controller) and receiver housing referred to in the image above as the "power pod". The wiring extends three inches back into the cabin where the battery is secured onto the cabin-section truss. It is secured in place via a fitted 3D printed nose plate and a wooden dowel skewered three quarters down the length of the pod. Two additional dowels were threaded behind and in front of the main wing, acting as anchor points for the four elastic bands bracing the wing to the top-deck of the fuselage.

Figure 23: Interior Airframe

Figure 24: Tail

Figure 25: Wing

Figure 25 shows the XPS wire cut foam wing after the vacuum bagging process. The foam core was prepared and sealed inside of a West System 106-206 slow-curing resin bath. After allowing 24 hours for the resin to cure, we removed the wing from the bag and trimmed the excess fibreglass away from the desired shape. Imperfections in the vacuum seal resulted a number of large, performance inhibiting blisters, particularly over the upper surface. These areas were sanded back down to the foam-core, patched with additional layers of fiberglass, and sanded once more for smoothness. UV-curing solar resin was used to similar effect were the smaller blisters occurred. The wing depicted above is actually the second wing that was fabricated. The first one included six-inch ailerons installed at each end, articulated with dual 9 gram servos mounted on the underside.

Figure 26: Final Assembly

4.7 Pixhawk Overview and Integration

Autopiloting composes a core purpose for this project and competition. The ability to thoroughly review the capabilities of our aircraft to a degree where third party systems could be accurately programmed to direct its flight path represents a competent understanding of both aerodynamics and control theory. For the purpose of outlining the needs set in selecting our auto-piloting system, the automation goals listed in section 2.3 are restated below:

- 3-Axis Autopilot with Altitude hold, Vertical Speed, and Indicated Airspeed modes (1 point)
- Sequential Waypoint Navigation (1 point)
- No-Fly Zone Avoidance (3 points)
- Target Identification (5 points)
- Automatic Payload Release (1 point)

Due to the various instruments required to achieve such a diverse set of tasks (airspeed sensor, GPS/compass, PWM controller, etc.), we determined a centralized, module-based system would be most effective if one was available. Therefore, in order to support the aircraft's need for data gathering and autonomous control, our group chose to utilize the Pixhawk 4, an advanced autopilot system developed by the UAV product manufacturer, Holybro. In the simplest definition, this product is an all-in-one, module-based logic board which utilizes data communicated from GPS and airspeed sensors to accurately execute mission plans provided by ground control. A flash memory card on-board the device is loaded with drivers which allow it to interface with third party piloting software as well as store basic telemetry data.

The wiring of the Pixhawk is straightforward, as each module is assigned a labeled port on the board. The assignments of each of the device's ports are labeled in **Figure 27**. In terms of our group's use case, we occupy ports 10, 11, 14, and 15, linking the radio control receiver, servo/ESC data, airspeed sensor and GPS module respectively. The servo/ESC data is an output module meant to provide continuity of a 3.3V logic input originating from the power management board (PMU).

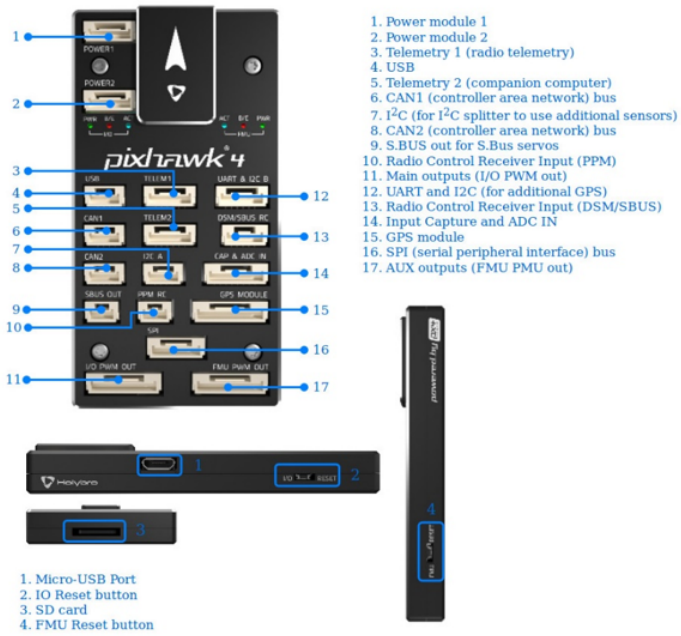

Figure 27: Port Mapping of the Pixhawk 4

All three voltage rails of the Pixhawk are delivered clean power from this module. +5V power is also delivered to the electronic speed controller (ESC) through soldered pads. The data line of this controller is routed from the battery eliminator circuit (BEC) to the PWM pins configured for throttle control and data collection into the Pixhawk's memory. Servos utilized for both elevator and rudder motion are plugged into the PWM pins alongside this BEC line. The wiring diagram for this configuration is illustrated in **Figure 28**.

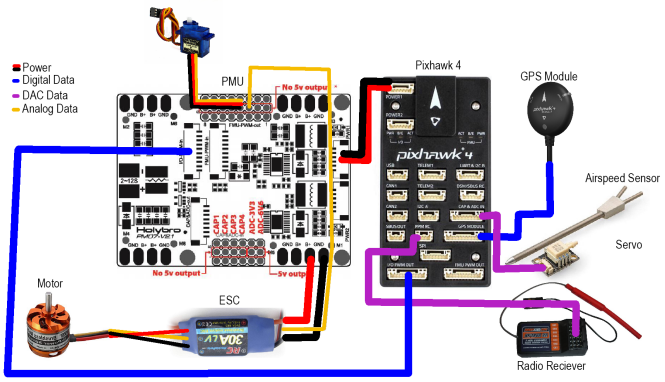

Figure 28: Wiring diagram of the aircraft's electrical systems

4.7.1 Mission Planner and ArduPilot

With our configuration, the entire system is fed power alongside an interconnected data network which is managed and recorded via ground control station (GCS) and autopiloting software. ArduPilot is one such autopiloting solution developed by 3DRobotics (3DR) and is the platform recommended by Holybro for use with most of their products including the Pixhawk 4. In order to access this software, it is loaded into the Ground Control Station (GCS) application, Mission Planner. During its initial setup, the application's graphic user interface (GUI) prompts the selection of firmware depending on the type of craft being developed. In our case, the fixed wing selection 'ArduPlane' shown in **Figure 29** was necessary.

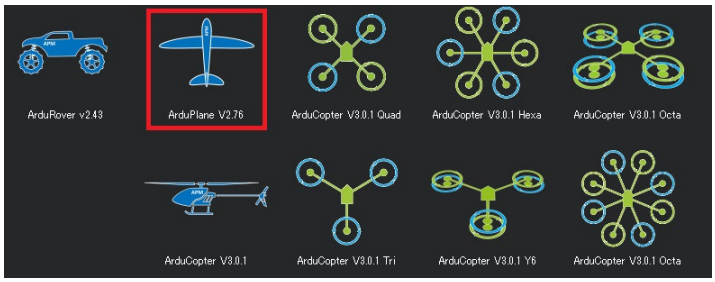

Figure 29: Firmware selection GUI from Mission Planner

After firmware is loaded, the Pixhawk can be synced over what the app defines as a 'MavLink' connection via a communication port (COM) such as USB. With this, all analog and digital data collection devices integrated with the Pixhawk will now communicate with ground control. A GPS map of the surrounding environment will be constructed, in which our group can define waypoints or unique flight paths as shown in **Figure 31**.

Figure 30: Waypoint mapping GUI from Mission Planner

The Pixhawk utilizes a satellite link with an on-board module in order to establish the aircraft's geo-coordinate. Once established, third party services such as Google Maps can be utilized to develop an accurate topographical map of the surrounding area which provides necessary data such as elevation in order to gauge altitude in-flight. For the purpose of explaining how the aforementioned function of the Pixhawk accomplishes our established auto-piloting goals, the following test was organized to take place on the WPI quad.

First, a satellite link would be established in order to develop an accurate map of the quad from our ground control station (GCS) within the Mission Planner computer program.

Once this map was generated, we would use the flight planning feature of Mission Planner to set waypoints at two points of the quad walkway. The point of takeoff set in front of the Sport's and Recreation Center's entrance, and the point of landing set at the closest point of the quad running counterclockwise around the area.

This system, fulfilling the goal of waypoint navigation, would also act as our primary method of achieving target identification and no-fly zone avoidance. If a designated flight plan is set, the plane will follow it so long as manual control is not re-established. Assuming the waypoint mapping stays within the flight boundaries and passes over the payload target area, all three respective goals would be reached.

Despite Ardupilot's handling of waypoint navigation along the established topographical area through purely automated handling of control surfaces, additional PWM operations can be executed to additional systems beyond flight control at specified waypoints. Our group intended to wire a solenoid in the payload bay responsible for restricting a spring-loaded release mechanism. Once the aircraft passed over the target waypoint, a PWM signal would be programmed to release the solenoid and drop the payload, thus achieving our goal of automated payload delivery. Although this particular application was not intended as an objective for this specific test, in the interest of establishing how the Pixhawk meets all five of our established goals, it was included in this summary.

To gauge the effectiveness of the Pixhawk's PWM signaling to our aircraft's control surfaces in meeting our goal of establishing a 3-Axis Autopilot, we would carry the vehicle along the flight plan while repeatedly directing it away from set waypoints. If functioning correctly, the servo motors should act to direct the control surfaces in a manner which would place the aircraft back on its pre-loaded flight plan. As to the outcome of these tests, due to the early closing of campus activities as a result of the spread of COVID-19, they were unable to be completed as planned.

4.8 Flight Test

The only flight test of the aircraft was conducted on March 7th at the Millis Model RC Airfield Club field in Medfield, Massachusetts. Unfortunately, by the time of the flight test, the ailerons had yet to

be installed in the main wing. We decided to guide the plane using only the tail's control surfaces, aware of the danger in doing so. With the absence of the payload bay, the plane was flown unloaded, enabling an easy hand-launch given our power to weight ratio.

As feared, a light lateral breeze induced a roll perturbance, followed by a tip-stall. With the inability to trigger a restorative roll, and insufficient altitude for a dive-recovery, the plane to a hard crash into the ground. A slight dihedral in the wing could have proven quite valuable in providing greater roll stability in lieu of ailerons.

Future computational stability analysis could be done to determine the optimal roll-stiffness given a variety of different configurations and geometries.

Fortunately, the cockpit section served as a long crimp-zone, absorbing the bulk of the impact, isolating most of the damage. All of the internal components remained intact. Having laser cut an extra copy, we were able to reconstruct the airframe within a day's time.

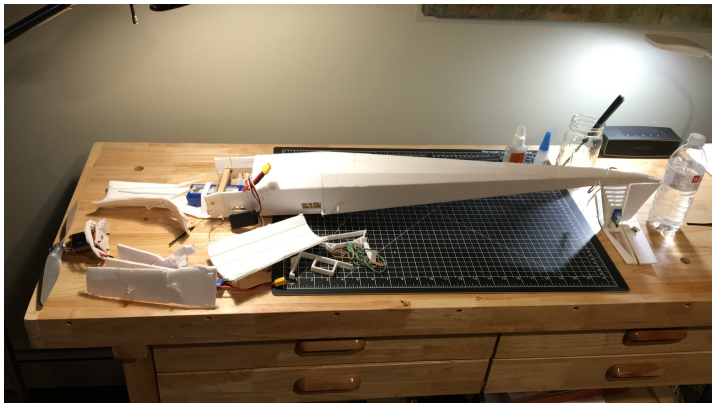

Figure 31: Fuselage Post - Mortem

5 Summary, Conclusions, Recommendations, Broader Impacts

5.1 Summary

This Major Qualifying Project consisted of the complete design and manufacturing of a functional micro-UAV for an internal WPI competition. In order to complete this task, first a literature review of previous UAVs and novel concepts was performed to gain a better understanding of this class of air vehicle. Once a decision was reached on an initial design, comprehensive analysis was performed to ensure the design was a successful one and it would be able to fly in the competition. This analysis began with an aerodynamic analysis of the chosen airfoil and wing design, ensuring that the aircraft had the required lift coefficient to maintain steady level flight. This involved a full drag analysis of the components of the aircraft as well. Then, structural analysis was performed under the assumption of a hollow, airfoil-shaped spar of fiberglass being the sole support for the wing. This assumption was made as the fiberglass reinforcement on the outside of the wing would have the largest structural influence by a large margin. Following the structural analysis was a short power analysis of the battery that would be placed in the aircraft. Finally, an analysis of the static and dynamic stability of the loaded aircraft was performed, which would influence weight placement and tail sizing.

Once a complete analysis was performed, fabrication of the aircraft could begin with a first prototype. Essentially this prototype was just a wing, fabricated to test the methods cutting the foam core and laying it up with fiberglass. After a few other trials, a final method was determined, cutting the core in two pieces and connecting them via a central support. Then the core was reinforced with 2-3 layers of fiberglass lay-up for major structural support. The fuselage was also fabricated at this time, using a method of folding foam board panels to provide a more streamlined polygonal surface, along

with a supporting truss placed in the payload bay (which contained opening doors) and a reinforced nose plate to hold the motor. The tail aerodynamic surfaces were 3-D printed for ease of manufacture. Prior to integration of the aircraft's control systems, a glide test was performed to test the structure's basic aerodynamic capabilities. To simulate the subtracted mass, a counterweight was affixed to the nose at the estimated mounting area for the autopilot and ESC. The craft was observed to stall when injected from altitude, however this was potentially due to imperfect simulation of weight distribution and the test was marked as inconclusive. Servos were attached to each control surface and interfaced through the receiver along with the motor. The Pixhawk autopilot was also chosen for ease of use and was configured to take control of the aircraft control surfaces to avoid the "no-fly zones" and keep the aircraft in a steady-state trim condition. It was also used in the hopes of directing the aircraft to the payload target autonomously. The final flight competition was cancelled due to the COVID-19 outbreak however, and thus the aircraft never flew past the testing phase.

5.2 Conclusions

This MQP resulted in a completed micro-UAV, but was not quite ready for the internal WPI competition at the time where the project was cut short by concerns about COVID-19. The construction methods that were used for the final product worked very well for the purpose of this project. The aircraft crashed during the first official test flight attended by the project advisors, but would have been easily salvageable. This is due to the fact that the fuselage was designed to be easily reproduced since it consisted of foam board panels that could be cut in very little time. If the project continued as normal, it would have been a simple task to rebuild the aircraft. The wing proved to be strong enough as well, as it was not damaged in the crash. With the final specifications given by the analysis portion of the project, the aircraft was both statically and dynamically stable and thus should have been able to fly at trim without much input from the pilot.

Overall, the team faced many challenges across the entire timeline of this project, including many structural and stability issues at the beginning of the design and manufacturing process. There were also a few supply chain issues with important components of the aircraft, which caused a delay in manufacturing. There was no solution to this issue besides waiting until the parts and supplies came in, and more options for suppliers might have been helpful to resolve this issue quickly. The rules required a loaded aircraft less than 3 kg, which usually would be a difficult constraint. However, constructing the aircraft out of foam board, XPS foam, and fiberglass allowed the aircraft to be much lighter than originally expected.The team was able to satisfy most of the competition rules in the design of our aircraft, though with a little bit more time, the team would definitely have been able to finalize an aircraft that satisfied all the rules and was capable of winning the competition.

5.3 Recommendations for Future Work

This section serves to recommend ways to make the process discussed in this paper much easier for anyone attempting to replicate it to build their own micro-UAV. Firstly, the team originally attempted to use novel ideas in the design of the aircraft, such as a ground-effect vehicle or an extremely high aspect ratio powered glider. It is advised to start with a more conventional design, as researching and performing the calculations for these types of vehicles took up a significant amount of time in the beginning of the project. Thus, with a simpler, more conventional design, more time can be spent on important design processes rather than designs that won't end up working.

Another recommendation is on the topic of wing fabrication. When cutting the wing the first few times, the team attempted to cut the entire thing at once followed by attempting to cut it in smaller sections. Neither method worked well and there were many voids and trailing edge defects. Thus, it is recommended that future wings be cut in two sections and glued together via a connecting support section. This method, along with using the hot wire foam cutter at a lower heat and slower speed will result in a cleaner cut and less structural defects on the wing.

The team also 3-D printed the tail aerodynamic surfaces due to a lack of time remaining and a constantly changing tail sizing. However, in order to reduce weight significantly, it is advised that the tail aerodynamic surfaces be manufactured in the same way as the main wing section. This would not only make it lighter, but also stronger compared to the 3-D printed version. Also, the team could not find an effective way to attach the vertical tail to the body of the aircraft and thus it might have been torn off in flight. It is recommended that a stronger fitting system be designed for structural support of the tail.

5.4 Project Broader Impacts

This project has revealed many potential applications for the use of micro-UAVs in real-world situations. For example, militaries around the world use larger unmanned aircraft for surveillance. Since smaller aircraft can be manufactured very easily as shown over the course of this project, they can be applied to this task as well in a greater number. However, it is not only a military application. Many civilian opportunities present themselves as well. These micro-UAVs can be used to monitor traffic situations and other important happenings in city infrastructure. They can also be used in natural disaster response, flying over dangerous areas with low visibility such as flood zones or wildfires and imaging the area to plan a safe path for ground response vehicles.

Micro-UAVs also present a commercial opportunity in the area of package delivery. Although a quadrotor aircraft or something similar with hover capability would be preferable, a fixed wing UAV could be used to deliver packages for online shoppers. A more reasonable use, however, would be their ability to deliver relief supplies to areas in need, such as natural disaster sites where ground vehicles cannot reach without extreme danger. The compact size of the aircraft is also a bonus in all of these areas, as they would be able to be transported much easier than larger unmanned aircraft and could access areas previously inaccessible to larger surveillance UAVs. Thus, this project demonstrates that micro-UAVs like the one built by the team could become increasingly common across all walks of life in the near future.

References

[1] Airfoil Database Search, 2019. http://airfoiltools.com/search/index [Accessed: 2019-09-15].

[2] ASM Material Data Sheet, 2019. http://asm.matweb.com/search/SpecificMaterial.asp?bassnum=MA6061T6 [Accessed: 2019-11-23].

[3] EPPLER 434 AIRFOIL (e434-il), 2019. http://airfoiltools.com/airfoil/details?airfoil=e434-il [Accessed: 2019-09-15].

[4] Mechanical Properties Data, 2019. http://www.mse.mtu.edu/ drjohn/my4150/props.html [Accessed: 2019-12-03].

[5] Properties: E-Glass Fibre, 2019. https://www.azom.com/properties.aspx?ArticleID=764 [Accessed: 2019-12-03].

[6] John J. Bertin and Michael L. Smith. *Aerodynamics for Engineers*. Prentice Hall, 3rd edition, 1998.

[7] Albion H. Bowers, Oscar J. Murillo, Robert Jensen, Brian Eslinger, and Christian Gelzer. On wings of the minimum induced drag: Spanload implications for aircraft and birds. Technical report, NASA, 2016.

[8] Paul Brickhill. *The Dam Busters*. Evans Brothers, 1951.

[9] Thomas P. J. Crompton. *Battery Reference Book*. Newnes, 3rd edition, 2000.

[10] David Hally. Calculation of the moments of polygons. Technical report, Defense Research Establishment Atlantic, 1987.

[11] Christoph Hiemcke. *Design of a wing section in ground effect: application to high speed ground transportation*. PhD thesis, Iowa State University, 1994.

[12] Robert M. Jones. *Mechanics of Composite Materials*. Taylor & Francis, 2nd edition.

[13] Daniel P. Raymer. *Aircraft Design: A conceptual Approach*. American Institute of Aeronautics and Astronautic Inc., 5th edition, 2012.

[14] Carlos J. Sarria, David William Irwin, Ethan Andrew Connors, James Allen Blair, and Keegan N. Mehrtens. Design of a micro class aircraft for the 2012 sae aero design east competition, mqp report, 2012.

[15] Herman Schlichting. *Boundary-Layer Theory*. McGraw Hill, 7 edition, 1979.

[16] Mohammad Tavakoli and Mohammad Saeed Seif. A practical method for investigation of aerodynamic and longitudinal static stability of wing-in-ground effect. *International Journal of Maritime Technology*, 4, 2015.

[17] Lance W Traub. Range and endurance estimates for battery-powered aircraft. Technical report, Embry-Riddle Aeronautical University, 2011.

[18] C. Wieselsberger. Technical report, National Advisory Committee for Aeronautics, 1922.

[19] Justin Winslow, Hikaru Otsuka, Bharath Govindarajan, and Inderjit Chopra. Basic understanding of airfoil characteristics at low reynolds numbers (10^4–10^5). $Journal of Aircraft, 55(3), 2018$.

6 Appendix A: Computer Code Used

6.1 Drag Analysis

```
import numpy as np
import matplotlib.pyplot as plt

dat = np.loadtxt('EPPLER 434 AIRFOIL 11t_T1_Re0.100_M0.00_N9.0_XtrTop50%.txt', \
     skiprows=11)
dat = np.transpose(dat)
alpha = dat[0,5:35]
AR = 10.
e = .9
L = 3*9.8 #N
S = 0.15 #m^2
rho = 1.22 #kg/m^3
cl = dat[1,5:35]
cd = dat[2,5:35]

cm = dat[4,5:35]

cD0 = cd + 0.0065

cL = cl*(AR/(AR+2.))

cDi = cL**2/(np.pi*AR*e)

cD = cDi + cD0

# L = q*cL*S = 30 N
q = L/(cL*S)
v = np.sqrt(2*q/(rho))


D = q*cD*S
Di = q*cDi*S
D0 = q*cD0*S

ldmax = np.argmin(D)
print('alpha_ldmax = ' + str(alpha[ldmax]))
print('D_ldmax = ' +str(D[ldmax]))
print('L/Dmax = ' +str(L/D[ldmax]))
print('L/D6 = ' +str(L/D[18]))
print('V_6 = ' +str(v[18]))
print('V_ldmax = ' +str(v[ldmax]))
print('q_ldmax = ' +str(q[ldmax]))


plt.plot(dat[0],dat[1], 'g-')
plt.title('C_l vs AOA')
plt.grid()
plt.axvline(x=alpha[ldmax],linestyle='-.',color='c')
plt.axhline(y=cl[ldmax],linestyle='-.',color='c')
plt.xlabel('AOA [deg]')
plt.ylabel('C_l')
plt.show()

plt.plot(alpha,cd, 'r-')
plt.title('2D C_d vs AOA')
plt.grid()
plt.axvline(x=alpha[ldmax],linestyle='-.',color='c')
plt.axhline(y=cd[ldmax],linestyle='-.',color='c')
plt.xlabel('AOA [deg]')
```

```
plt.ylabel('C_d')
plt.show()

plt.plot(v,D, 'm-')
plt.plot(v,Di, 'b-')
plt.plot(v,D0, 'r-')
plt.title('D vs v')
plt.grid()
plt.legend()
plt.axvline(x=v[ldmax],linestyle='-.',color='c')
plt.axhline(y=D[ldmax],linestyle='-.',color='c')
plt.xlabel('V [m/s]')
plt.ylabel('D [N]')
plt.show()
```

6.2 Airfoil 2nd Moment of Ineria Analysis

```
from numpy import *
xy = loadtxt('EPPLER 434 AIRFOIL 11t.dat', skiprows = 1)
x_c = xy[:,0]
y_c = xy[:,1]
#NOTE this program computes the 2nd moment of inertia about the chord line
n = 3. #number of layers
t_l = 7.62e-5 #m, thickness of an individual layer, taken from lower bound of spec

t = n*t_l #structure thickness

def iy(x,y,c,t):
    iy = 0.
    x = x_c*c
    y = y_c*c
    #break up airfoil into series of paralellograms and find moment of inertia of each
    #polygon has sides paralel to the x axis
    dx = diff(x)
    dy = diff(y)
    m = dy/dx
    del_y = t * cos(arctan(m))
    for i in range(size(x[:-1])):
        p1 = [x[i],y[i]]
        p2 = [x[i+1],y[i+1]]
        p3 = [x[i+1],y[i+1]+del_y[i]]
        p4 = [x[i],y[i]+del_y[i]]
        a1 = (1./12.)*(p1[0]*p2[1]-p2[0]*p1[1])*(p1[1]**2+p1[1]*p2[1]+p2[1]**2)
        a2 = (1./12.)*(p2[0]*p3[1]-p3[0]*p2[1])*(p2[1]**2+p2[1]*p3[1]+p3[1]**2)
        a3 = (1./12.)*(p3[0]*p4[1]-p4[0]*p3[1])*(p3[1]**2+p3[1]*p4[1]+p4[1]**2)
        a4 = (1./12.)*(p4[0]*p1[1]-p1[0]*p4[1])*(p4[1]**2+p4[1]*p1[1]+p1[1]**2)

        iy += a1 + a2 + a3 + a4
    return(abs(iy))

z_range = linspace(0.,.6,100)
#c = .1708+z_range*(.0732-.1708)/.6
iy_c = []
for z in z_range:
    iy_c = iy_c + [iy(x_c,y_c,.1708+z*(.0732-.1708)/.6,t)]
out = transpose(asarray([z_range,iy_c]))
savetxt("iy_of_y.csv", out, delimiter=",")
```

6.3 Stability Matlab Code

```
clear variables; close all; clc;

%% Flight condition

u_0 = 72.1785;      % ft/s
rho = 0.0023769;    % slug/ft^3
g   = 32.2;     % ft/s^2
theta_0 = 0;    % rad

%% Aircraft data

%----- Geometry
machord     = 0.4002625;    % ft
wing_span   = 3.93701;  % ft
S           = 1.61459;  % ft^2

%----- Inertia
weight      = 6.61387;      % lb
mass        = weight/g; % slug
I_x         = 0;    % slug.ft^2
I_y         = 0.3670;
I_z         = 0;
I_zx        = 0;

%----- Longitudinal steady state coefficients
C_L_1       = 0.8313;
C_D_1       = 0.0489;
C_m_1       = 0;
C_T_x1      = 0;
C_m_T1      = 0;

%----- Longitudinal stability derviatives
C_D_u       = 0;
C_D_alpha   = 0.4437;
C_L_u       = 0.0034;
C_L_alpha   = 7.708;
C_L_alpha_d = 1.5020;
C_L_q       = 17.0426;
C_m_alpha   = -7.4396;
C_m_alpha_d = -7.0265;
C_m_q       = -73.1540;
C_m_0       = 0.0;
C_m_u1      = 0.0;
C_m_Tu      = 0;
C_T_xu      = 0;

%----- Longitudinal control derivatives
C_D_de      = 0;
C_L_de      = 0;
C_m_de      = 0;

%----- Lateral stability derviatives
C_y_beta    = -0.59;
C_y_p       = -0.19;
C_y_r       = 0.39;
C_l_beta    = -0.13;
C_l_p       = -0.50;
C_l_r       = 0.14;
C_n_beta    = 0.08;
C_n_p       = 0.019;
C_n_r       = -0.197;

%----- Lateral control derivatives
C_y_da      = 0;
```

```
C_y_dr      = 0.144;
C_l_da      = 0.156;
C_l_dr      = 0.01016;
C_n_da      = -0.0012;
C_n_dr      = -0.0758;

%% Nondimensional

C_w0        = weight / ( 0.5*rho*u_0^2*S );

%----- Longitudinal
C_x_u       = -( C_D_u + 2*C_D_1 );
C_x_alpha   = C_L_1 - C_D_alpha;
C_x_alpha_d = 0;
C_x_q       = 0;
C_x_de      = -C_D_de;
C_x_dp      = C_T_xu + 2*C_T_x1;

C_z_u       = -( C_L_u + 2*C_L_1 );
C_z_alpha   = -( C_L_alpha + C_D_1 );
C_z_alpha_d = -C_L_alpha_d;
C_z_q       = -C_L_q;
C_z_de      = -C_L_de;
C_z_dp      = 0;

C_m_u       = C_m_u1 + 2*C_m_1;
C_m_dp      = C_m_Tu + 2*C_m_T1;

%% Derivatives

%----- Longitudinal
X_u     = rho*u_0*S*C_w0*sin(theta_0) + 0.5*rho*u_0*S*C_x_u;
X_w     = 0.5*rho*u_0*S*C_x_alpha;
X_q     = 0.25*rho*u_0*S*machord*C_x_q;
X_w_d   = 0.25*rho*S*machord*C_x_alpha_d;
X_de    = 0.5*rho*u_0^2*S*C_x_de;
X_dp    = 0.5*rho*u_0^2*S*C_x_dp;

Z_u     = -rho*u_0*S*C_w0*cos(theta_0) + 0.5*rho*u_0*S*C_z_u;
Z_w     = 0.5*rho*u_0*S*C_z_alpha;
Z_q     = 0.25*rho*u_0*S*machord*C_z_q;
Z_w_d   = 0.25*rho*S*machord*C_z_alpha_d;
Z_de    = 0.5*rho*u_0^2*S*C_z_de;
Z_dp    = 0.5*rho*u_0^2*S*C_z_dp;

M_u     = 0.5*rho*u_0*S*machord*C_m_u;
M_w     = 0.5*rho*u_0*S*machord*C_m_alpha;
M_q     = 0.25*rho*u_0*S*machord^2*C_m_q;
M_w_d   = 0.25*rho*machord^2*S*C_m_alpha_d;
M_de    = 0.5*rho*u_0^2*S*machord*C_m_de;
M_dp    = 0.5*rho*u_0^2*S*machord*C_m_dp;

%----- Lateral
Y_v     = 0.5*rho*u_0*S*C_y_beta;
Y_p     = 0.25*rho*u_0*S*wing_span*C_y_p;
Y_r     = 0.25*rho*u_0*S*wing_span*C_y_r;
Y_da    = 0.5*rho*u_0^2*S*C_y_da;
Y_dr    = 0.5*rho*u_0^2*S*C_y_dr;

L_v     = 0.5*rho*u_0*S*wing_span*C_l_beta;
L_p     = 0.25*rho*u_0*S*wing_span^2*C_l_p;
L_r     = 0.25*rho*u_0*S*wing_span^2*C_l_r;
L_da    = 0.5*rho*u_0^2*S*wing_span*C_l_da;
L_dr    = 0.5*rho*u_0^2*S*wing_span*C_l_dr;

```

```
N_v     = 0.5*rho*u_0*S*wing_span*C_n_beta;
N_p     = 0.25*rho*u_0*S*wing_span^2*C_n_p;
N_r     = 0.25*rho*u_0*S*wing_span^2*C_n_r;
N_da    = 0.5*rho*u_0^2*S*wing_span*C_n_da;
N_dr    = 0.5*rho*u_0^2*S*wing_span*C_n_dr;

%% Linearization

qty1 = mass - Z_w_d;
qty2 = M_w_d/qty1;
%qty3 = I_x*I_z - I_zx^2;
qty4 = Z_q + mass*u_0;
%I_xp = qty3 / I_z;
%I_zp = qty3 / I_x;
%I_zxp= I_zx / qty3;

A_long  = [...
    X_u/mass                X_w/mass                0                       ...
        -g*cos(theta_0); ...
    Z_u/qty1                Z_w/qty1                qty4/qty1               ...
        -weight*sin(theta_0)/qty1; ...
    (M_u + qty2*Z_u)/I_y    (M_w + qty2*Z_w)/I_y    (M_q + qty2*qty4)/I_y   ...
        -qty2*weight*sin(theta_0)/I_y;
    0                       0                       1                       0]

%
de_trim = -(C_m_0*C_L_alpha + C_m_alpha*C_L_1) / (C_L_alpha*C_m_de - C_L_de*C_m_alpha);

eig(A_long)



%% Longitudinal trim
C_L_trim= C_w0;

de_trim = -(C_m_0*C_L_alpha + C_m_alpha*C_L_trim) / (C_L_alpha*C_m_de - ...
    C_L_de*C_L_alpha)
de_trim*180/pi


%% Disturbance responses
[t_sim, xi_sim] = ode45(@(t,xi) A_long*xi, [0 200], [3*randn 0 0 0]');
figure('Name', 'Response to speed disturbance');
subplot(411)
plot(t_sim, xi_sim(:, 1))
xlabel('t (s)'); ylabel('\Delta u ft/s'); grid on;

subplot(412)
plot(t_sim, xi_sim(:, 2))
xlabel('t (s)'); ylabel('w ft/s'); grid on;

subplot(413)
plot(t_sim, xi_sim(:, 3)*180/pi)
xlabel('t (s)'); ylabel('q \circ/s'); grid on;

subplot(414)
plot(t_sim, xi_sim(:, 4)*180/pi)
xlabel('t (s)'); ylabel('\Delta \theta \circ'); grid on;

% print -dpng long_open_loop_speed.png


[t_sim, xi_sim] = ode45(@(t,xi) A_long*xi, [0 200], [0 2*randn 0 0]');
figure('Name', 'Response to angle of attack disturbance');
subplot(411)
```

```
plot(t_sim, xi_sim(:, 1))
xlabel('t (s)'); ylabel('\Delta u ft/s'); grid on;

subplot(412)
plot(t_sim, xi_sim(:, 2))
xlabel('t (s)'); ylabel('w ft/s'); grid on;

subplot(413)
plot(t_sim, xi_sim(:, 3)*180/pi)
xlabel('t (s)'); ylabel('q \circ/s'); grid on;

subplot(414)
plot(t_sim, xi_sim(:, 4)*180/pi)
xlabel('t (s)'); ylabel('\Delta \theta \circ'); grid on;



[t_sim, xi_sim] = ode45(@(t,xi) A_long*xi, [0 200], [0 0 0 (5*randn*pi/180)]');
figure('Name', 'Response to pitch disturbance');
subplot(411)
plot(t_sim, xi_sim(:, 1))
xlabel('t (s)'); ylabel('\Delta u ft/s'); grid on;

subplot(412)
plot(t_sim, xi_sim(:, 2))
xlabel('t (s)'); ylabel('w ft/s'); grid on;

subplot(413)
plot(t_sim, xi_sim(:, 3)*180/pi)
xlabel('t (s)'); ylabel('q \circ/s'); grid on;

subplot(414)
plot(t_sim, xi_sim(:, 4)*180/pi)
xlabel('t (s)'); ylabel('\Delta \theta \circ'); grid on;


% print -dpng long_open_loop_aoa.png
```

7 Appendix B: WPI UAV Competition Rules

2020 WPI UAV COMPETITION RULES

1. Mission Requirements

The aircraft's mission is to take-off from a specified take-off/landing area, deliver payload at a specified target location, and return and land in the take-off/landing area. The aircraft's ability to perform this mission will be scored based on the aircraft's range, maximum payload, accuracy of delivery, autonomy of the mission, and originality of the aircraft design (see scoring metric details in Section 3).

Competing designs are limited to fixed wing aircraft only for Profs Olinger and Jayachandran teams, and rotating wing/blade aircraft for Prof. Cowlagi's team. All parts of the aircraft must be either sourced from salvaged parts of previous WPI projects or purchased through WPI-provided funds for the MQP. Students' personal funds may not be used to purchase any hardware or software parts of the aircraft.

1.1 Venue

The competition will be conducted outdoors and away from the WPI campus, e.g., at an airfield maintained by a model aircraft club or similar airfield. Teams should be prepared to transport the designed aircraft by car to the competition venue. Teams will have the opportunity to scout the venue and/or conduct flight tests at the venue before the day of the competition.

1.2 Payload and Delivery

Payload will be in the form of standard beanbags (Amazon link: : https://www.amazon.com/dp/B07DRNLCYD/ref=cm_sw_em_r_mt_dp_U_YSRBDbDN5GMJ5), and must be air-dropped to the target location. Students may not modify the beanbags except by removing some portion of the filling sand, however all sand used as payload weight must be contained in a beanbag. The beanbags used as payload will be weighed just prior to all qualifying and competition flights. The payload beanbags must be fastened together into a single unit for the air-drop. A soft, flexible structure may be used to carry the payload beanbags external to the aircraft, for example in a 'sling load' beneath the aircraft. This structure will count as empty weight (not payload weight).

1.3 Target Demarcation

The target location for payload delivery will be indicated by visibly distinctive markings on the ground. GPS coordinates of the target will be provided, as measured using a typical smartphone GPS receiver, i.e., typical GPS-based localization errors are to be expected. In addition to these two identifiers (visible markings and GPS coordinates), each team will be allowed to place up to one identification aid on the target on the day of the competition. Typical aids include QR codes/April tags, a bright navigation light, and radio beacons. This identification aid must receive approval from the judges no later than January 20, 2019, and must be described in the final project report prior to the day of the competition.

The general airfield layout is shown in the following figure.

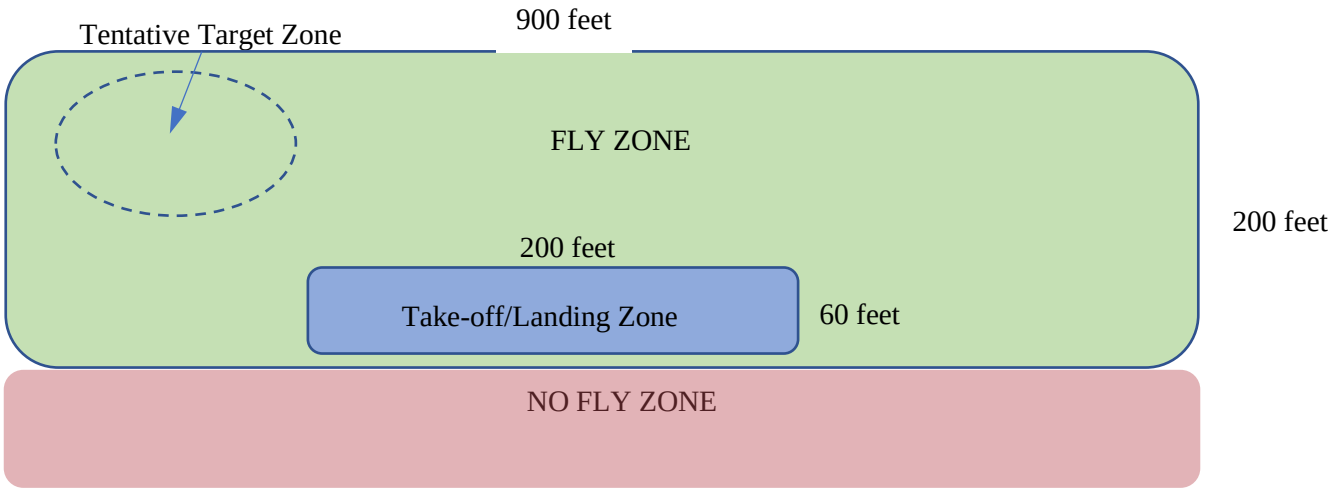

Plan of Airfield

1.4 No-Fly Zones

- Specific no-fly zones will be defined for the competition venue (see figure above).
- At no time will an aircraft enter the no-fly zones, whether under controlled flight or uncontrolled.
- At no time will an aircraft's altitude exceed 100 m above ground level.
- First infraction for crossing into the no-fly zone will result in an invalidated flight attempt and zero points will be awarded for that flight.
- Second infraction will result in disqualification from the entire event and loss of all points.
- It is the team and team pilot's responsibility to be aware of the venue-specific no-fly zones and to comply with all venue specific rules.
- If a team is unable to directionally control their aircraft and it is headed towards or is in a no-fly zone, the judges may order the pilot to intentionally crash the aircraft to prevent it from endangering people or property. This safety directive must be followed immediately if so ordered.
- GPS coordinates of the corners of the fly zone (green region in the above figure) will be provided.

1.5 Take-off

Allowable methods of take-off include hand launch, ground roll, and catapult launch. The take-off method should account for the possibility of snow cover on the ground. The aircraft must climb to an observable ground clearance (see Section 1.6) by the end of the take-off zone. An aircraft that 'touches down' within the take-off zone after initial launch but still attains this observable take-off ground clearance completes a successful take-off.

1.6 Flight

The aircraft must fly at an observable ground clearance (distance between lowest point on aircraft including external payload and the ground) throughout the flight between take-off and landing. A judge using normal vision standing in the take-off/landing zone must be able to observe this ground clearance OR the team must independently provide clear evidence that this rule is met within 10 minutes after the

completion of the flight. A flight will be considered as immediately terminated for scoring purposes the first time this rule is violated outside the take-off/landing zone.

1.7 Landing

- The take-off/landing zone will be visibly marked.
- It is the team and team pilot's responsibility to be aware of the class specific landing zone dimensions at the event site.
- All aircraft must remain within the designated landing zone runway during landing. Any aircraft that leaves their designated landing zone during landing are subject to a penalty of 50% of any points earned during the flight prior to landing.
- Any flight where the aircraft does not make the initial touch down for landing inside the designated landing zone is disqualified and forfeits all points for that flight.
- Any landing where the aircraft is not rolling or sliding on the ground when it leaves the landing zone (i.e., bouncing into the air as it leaves the landing zone) is disqualified. Touch-and-go landings are not allowed and will be judged as a failed landing attempt.
- The criteria for being within the landing zone is that no supporting part of the aircraft that is touching the ground can be outside the landing zone. For example, a wing tip or fuselage is allowed to overhang the edge of the landing zone, as long as no supporting part of the aircraft is physically touching anything outside the landing zone.

1.8 Autonomy

~~Commercially available systems use?~~ Yes, budget permitting

Autonomous flight may be demonstrated in one or more of the following capabilities of the aircraft while the pilot exerts no remote control. For any of these capabilities to be adjudicated as "autonomous" for any duration of flight, the pilot's hands must remain visible and out of contact with the controls throughout that duration.

1. **Autopilot:** the aircraft maintains steady flight (e.g., constant altitude and/or constant airspeed, or constant rate of climb / descent).
2. **Waypoint guidance:** the aircraft travels through a sequence of spatial waypoints. These waypoints may be specified in terms of geographic coordinates (e.g., latitude-longitude) encoded in software, or indicated on a map through a graphic user interface, or indicated by ground-based markers to be detected by the aircraft during flight.
3. **No-fly zone avoidance:** the aircraft plans and executes maneuvers to avoid no-fly zones. Autonomous traversal along a preplanned sequence of waypoints that already avoid the no-fly zone will not be counted as a demonstration of no-fly zone avoidance capability.
4. **Target detection:** the aircraft detects the target location on the ground using visibly distinctive markings to identify the target.
5. **Payload drop:** the payload is autonomously released from the aircraft without the pilot's manual activation of a switch.

1.9 Originality of Design

Originality of the design will be judged based on differences in overall aircraft configuration compared to WPI SAE micro-aircraft or WPI VTOL drones that have been developed in previous WPI MQP projects or graduate project work.

1.10 On the Day of the Competition

No changes to aircraft except ballast adjustments and replacement of batteries and/or propellers will be allowed after reaching the competition venue on the day of the competition. To qualify for the competition, teams must demonstrate before the day of the competition:

- Take-off and landing (as described in Sections 1.5 and 1.6) and at least **one minute** of flight time with an empty aircraft.
- Take-off and landing (as described in Sections 1.5 and 1.6) and at least **one minute** of flight time with half of the design payload (see Section 5.6).

See Section 5.8 for flight test reporting requirements.

1.11 Judges

The faculty advisors on the UAV MQP projects will serve as judges during the flight competition and to interpret competition rules throughout the MQP projects.

2 Design Constraints

2.1 Empty CG

All aircraft must meet the following Center of Gravity (CG) related requirements:

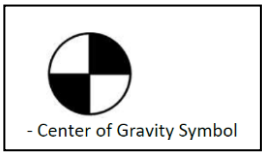
- Center of Gravity Symbol

- All aircraft must be flyable at their designated Empty CG position (no payload, ready to fly).
- All aircraft must have the fuselage clearly marked on both sides with a classic CG symbol (below) that is a minimum of 0.5 inches in diameter centered at the Empty CG position (Wing type aircraft may place the two CG markings on the bottom of the wing.)

2.2 Gross Weight Limit

Aircraft gross take-off weight including payload may not exceed 3 kg.

2.3 Controllability

All aircraft must be remotely controllable at all times during flight.

2.4 Radio Control System

The use of a 2.4 GHz radio control system is required for all aircraft. The 2.4 GHz radio control system must have a functional fail-safe system that will reduce the throttle to zero if the radio signal is lost.

2.5 Spinners or Safety Nuts Required

All powered aircraft must utilize either a spinner or a rounded model aircraft type safety nut.

2.6 Metal Propellers

Metal propellers are not allowed.

2.7 Lead is Prohibited

The use of lead in any portion of any aircraft (payload included) is strictly prohibited.

2.8 Payload Distribution

The payload cannot contribute to the structural integrity of the airframe.

2.9 Aircraft Ballast

Aircraft ballast, defined as non-payload weight needed to alter CG location, is allowed with the following conditions:

- Ballast cannot be used in a closed payload bay
- Ballast locations must be clearly indicated on the 2D drawings in MQP report.
- Ballast must be secured so as to avoid shifting or falling off the aircraft, thereby shifting the CG.
- Ballast will not be counted as payload.

2.10 Stored Energy Restriction

Aircraft must be powered by electric motors on board the aircraft. No other internal forms of stored potential energy allowed on the aircraft Stored potential or elastic energy is allowed in a catapult launch mechanism.

2.11 Control Surface Slop

Aircraft control surfaces and linkage must not feature excessive slop. Sloppy control surfaces lead to reduced controllability in mild cases, or control surface flutter in severe cases.

2.12 Servo Sizing

Analysis and/or testing must be described in the Design Report that demonstrates the servos are adequately sized to handle the expected aerodynamic loads during flight.

2.13 Clevis Keepers

All control clevises must have additional mechanical keepers to prevent accidental opening of the control clevis in flight.

2.14 Red Arming Plug

All electric powered aircraft must use a discrete and removable red arming plug to arm and disarm the aircraft propulsion system. This red arming plug must be integrated into the electrical circuit between the battery and the electronic speed controller (ESC).

- The red arming plug must physically be located at 40% to 60% of the aircraft length from the aircraft propeller. This is to allow arming and disarming the aircraft at a safe distance from the propeller.
- The red arming plug must be located on top of the fuselage or wing and external of the aircraft surface.
- The location of the red arming plug must be clearly visible.
- The non-removable portion of the arming plug interface may not have more than one male lead.
- Disconnecting wiring harnesses to arm and disarm a system will **not** be allowed.

2.15 Battery Protection

- All batteries in the aircraft must be positively secured so that they cannot move under normal flight loads.
- The battery bay or location in the aircraft must be free of any hardware or other protrusions that could penetrate the battery in the event of a crash.

2.16 Power Limiter

All aircraft must use a 1000 W power limiter such as the one available here: https://neumotors.cartloom.com/storefront/product/24377.

2.17 Aircraft Systems Requirements

- Propulsion requirements: aircraft are restricted to electric motor propulsion only.
- Propeller and gearbox: gearboxes on an aircraft where the propeller RPM differs from the motor RPM are allowed. Multiple motors, multiple propellers, propeller shrouds, and ducted fans are allowed.
- The aircraft should use Lithium Polymer batteries. The maximum size propulsion system battery allowed is a 3-cell 2200 mAh lithium polymer battery. Batteries having fewer cells and lower capacity are permitted.
- Gyroscopic assist and other forms of stability augmentation are allowed.
- Aircraft empty weight definition: All aircraft parts that are not payload contribute to the empty aircraft weight, including, but not limited to: airframe, receiver, electronics, batteries, hardware, brackets, straps and other associated features.

3 Scoring Metric

To receive a score on the day of the competition, teams must demonstrate the following flight sequence: take-off, complete range leg (flight time t_{flight} from take-off to drop used in scoring equation), drop payload, return and land. The flight score S is given by the following equation. The highest flight score among at most three attempts on the day of the competition will be considered.

$$S = \lambda_1 \frac{W_{\text{payload}}}{W_{\text{empty}}} \cdot t_{\text{flight}} \cdot V_{avg} + \lambda_2 \Delta + \lambda_3 \sum_n A_n + P.$$

Symbol	Meaning
$W_{\text{loaded}}, W_{\text{empty}}$	Weight of the aircraft with and without payload, respectively
t_{flight}	Time of flight in range leg in secs
V_{avg}	Average groundspeed during flight, computed using onboard GPS-based speed measurements in meters/sec.
Δ	Define δ to be the distance between the target location and actual payload drop point. Then $\Delta = \begin{cases} 1, & 0 < \delta < 1\text{ m}, \\ 0, & 1\text{ m} \le \delta < 3.5\text{m}, \\ -1, & 3.5\text{m} < \delta. \end{cases}$

A_n	Points for demonstrating autonomy capabilities $n = 1, \dots, 5$ (see Section 1.8~~1.7~~) $A_1 = A_2 = A_5 = 1,$ $A_3 = 3,$ $A_4 = 5.$
P	Originality points on a scale of $0 - 10$.
λ_i	Constants $\lambda_1 = 0.01$, $\lambda_2 = 35$, and $\lambda_3 = 35$.

4 Operational Safety Requirements

4.1 Ground Safety and Flight Line Safety Equipment

- No open toe shoes allowed. All team participants, including faculty advisors and pilots, will be required to wear closed-toe shoes during flight testing and during flight competition.
- All students involved at the flight line launching aircraft must wear safety glasses and hard hats.
- The University name must be clearly displayed on the wings or fuselage.
- The University initials may be substituted in lieu of the University name provided the initials are unique and recognizable.

4.2 Team Pilots

All pilots must be current members of the Academy of Model Aeronautics or the Model Aircraft Association of Canada (AMA has an agreement with MAAC).

A current WPI student who meets this requirement is available to MQP teams. If an MQP student on a team is an experienced RC pilot and AMA member, they can serve as the pilot. However, MQP teams should not plan on training an inexperienced student.

4.3 Aircraft Configuration during Flight

The aircraft must remain intact during a flight attempt to receive full flight score. A flight attempt includes activities at the starting line, the take-off roll, takeoff, flight, landing and recovery after landing.

A 25% deduction from the flight score will be assessed if any of the following items are observed to completely detach from the aircraft during a flight attempt.

- Stickers
- Tape
- Coverings

With the exception of a broken prop during landing, if any other components fall off the during a flight attempt, the flight will be disqualified.

5 Reporting Requirements

5.1 2D Drawing Requirements

*Updated 2D drawings should be provided by each team to faculty advisors periodically throughout the project **and** in all draft MQP report submissions.*

5.2 2D Format and Size

The 2D drawing must be ANSI B sized page (PDF) format (11 x 17 inches). The drawing shall consist of one (1) page.

5.3 Views Required

Drawings shall include at a minimum, a standard aeronautical 3-view orthographic projection arranged as described:

- Left side view, in lower left, with nose pointed left.
- Top view, above and aligned with the left side view, also with nose pointed left (wing-span break-view permitted).
- Front view aligned to side view, located in the lower right (projection view nonstandard movement as noted by projection view arrows in accordance with ANSIY14.5M 1994).

5.4 Dimensions Required

Drawing dimensions and tolerance shall be in SI units, decimal notation accordance with ANSI-Y14.5M 1994 to an appropriate level of precision to account for construction tolerances (allowable variation from analyzed prediction to account for fabrication) (i.e. X.X = ± .1 cm; X.XX = ± .03 cm; X.XXX = ± .010 cm). The minimum required dimensions/tolerances are: Aircraft length, width, and height.

5.5 Summary Data Required

The drawing shall contain a summary table of pertinent data to include but not limited to:

- Wingspan
- Empty weight
- Battery(s) capacity
- Motor make and model
- Motor KV (micro and Regular Class only)
- Propeller manufacturer, diameter, and pitch
- Servo manufacturer, model number and torque specification in ounce-inches for each servo used on the aircraft. Identify servo being used at each position on the aircraft.

5.6 Weight and Balance Information

The 2D drawing shall contain the following weight, balance and stability information:

- A clearly marked and labeled aircraft datum.
- A weight and balance table containing pertinent aircraft equipment. Each item listed must show its location from the aircraft datum in centimeters (the moment arm), the force, and resultant moment. The minimum list of pertinent equipment includes:
    - Motor
    - Battery(s)
    - Payload

    - Ballast (if used)
    - Electronics
- Design maximum payload, and design payload for maximum range
- Aircraft mean aerodynamic chord, stability margin and CG information listed below must be clearly shown on drawing:
    - Aircraft mean aerodynamic chord
    - Stability margin for loaded CG and empty CG
    - Empty CG location (flightworthy)
    - Fully loaded CG (flightworthy, with payload, if applicable)

5.7 Tech Data Sheet: Weight Buildup

Updated Weight Buildup List should be provided by each team to faculty advisors periodically throughout the project **and** in all draft MQP report submission.

The Micro Class Weight & Balance Build-up List will help teams understand the importance of managing aircraft weight to achieve safety of flight at the desired payload fraction. Each team shall supply a one (1) sheet summary list of aircraft parts, part weight, and part weight percentage) that contribute to the overall empty weight of the aircraft.

5.8 Flight Tests

A flight test is an experiment conducted to study/demonstrate the real-world characteristics of an aircraft. For this competition, flight test evidence **must** be recorded by **both** of the following means:

- **Video** recorded from the ground.
- **Inertial measurements** recorded from an onboard inertial measurement unit. The following quantities must be recorded: body-axis angular velocities, body-axis accelerations, angular orientations, GPS position, GPS velocity.

In addition, optionally, video from an onboard camera may be recorded. Any flight experiment with only video evidence (i.e., inertial measurements log absent) will not be considered for reporting or qualifying requirements.

An unpowered glide flight test is required for the B-term MQP report. In addition, the following flight tests are required for a team to qualify for the competition:

- Take-off and landing (as described in Sections 1.5 and 1.6) and at least **one minute** of flight time with an empty aircraft.
- Take-off and landing (as described in Sections 1.5 and 1.6) and at least **one minute** of flight time with half of the design payload.